Study of Spontaneous Activity in the Peripheral Structure of Developing Mouse Somatosensory System

Banerjee, Piu

Supervisor: **Dr. Takuji Iwasato**

Doctor of Philosophy

December’ 2022

Department of Genetics
School of Life Science
The Graduate University for Advanced Studies,
SOKENDAI

Table of Contents

SUMMARY

Spontaneous activity during the early postnatal period is thought to be crucial for the establishment of mature neural circuits. It remains unclear if the peripheral structure of the developing somatosensory system exhibits spontaneous activity, similar to that observed in the retina and cochlea of developing mammals. By establishing an *ex vivo* calcium imaging system, here I found that neurons in the whisker-innervating region of the trigeminal ganglion (TG) of neonatal mice generate spontaneous activity. A small percentage of neurons showed some obvious correlated activity, and these neurons were mostly located close to one another. TG spontaneous activity was majorly exhibited by medium-to-large diameter neurons, a characteristic of mechanosensory neurons, and was blocked by chelation of extracellular calcium. Moreover, this activity was diminished by the adult stage. Spontaneous activity in the TG during the first postnatal week could be a source of spontaneous activity observed in the neonatal mouse barrel cortex.

INTRODUCTION

Studying the construction of mature neural circuits is crucial to comprehending their complexities. In the embryonic stage, genetic factors contribute to laying down the coarse neural networks, which are then refined postnatally by neuronal activity. In the developing mammalian brain, without any stimulus from the environment (e.g., light, sound, touch), the sensory cortices exhibit spontaneous activity, where groups of cells fire together in a specific spatiotemporal pattern and synchronization. Mostly, such synchronization disappears by the later postnatal stages (Kandler, Clause et al. 2009, Ackman, Burbridge et al. 2012, Cang and Feldheim 2013, Kirkby, Sack et al. 2013, Mizuno, Ikezoe et al. 2018, Nakazawa, Yoshimura et al. 2020, Martini, Guillamón-Vivancos et al. 2021, Nakazawa and Iwasato 2021). Accumulating evidence suggests that such correlated spontaneous activity plays an important role in the refinement of immature neural circuits following the Hebbian principles of plasticity, where synapses between co-active cells are further strengthened, and those within minimally active cells are weakened. This way, it prepares the circuit for future sensory processing (Katz and Shatz 1996, Yamamoto and López-Bendito 2012, Leighton and Lohmann 2016).

Among the developing sensory cortices, spontaneous activity was first identified in the mammalian visual cortex. In the visual cortex, spontaneous activity is observed during the early postnatal period, which propagates tangentially in a wave-like manner (Hanganu, Ben-Ari et al. 2006, Ackman, Burbridge et al. 2012). This activity originates from the retina, wherein the wave-type spontaneous activity was first discovered *in vitro* (Galli and Maffei 1988, Meister, Wong et al. 1991, Wong, Meister et al. 1993, Wong, Chernjavsky et al. 1995,

Ackman, Burbridge et al. 2012, Shen and Colonnese 2016). Similarly, in the auditory cortex, spontaneous activity is observed during the early postnatal period, which resembles the future tonotopic axis (Babola, Li et al. 2018). This activity originates from the cochlea, wherein spontaneous bursts of action potentials were first found *ex vivo* (Walsh and McGee 1987, Lippe 1994, Glowatzki and Fuchs 2002, Jones, Leake et al. 2007, Tritsch, Yi et al. 2007, Tritsch, Rodríguez-Contreras et al. 2010, Johnson, Eckrich et al. 2011, Leighton and Lohmann 2016, Martini, Guillamón-Vivancos et al. 2021). Hence, in the developing visual and auditory systems, the spontaneous activity in the cortices originates from their respective peripheral structures. In the somatosensory cortex (barrel cortex), the arrangement of barrels mirrors the pattern of facial whiskers, where each barrel receives input from a single whisker. During the first postnatal week, the layer 4 (L4) excitatory neurons of barrel cortex exhibit spontaneous activity where neurons within the same barrel fire together, thereby giving a patchwork-like appearance (Golshani, Gonçalves et al. 2009, Yang, Hanganu-Opatz et al. 2009, Yang, An et al. 2013, Mizuno, Ikezoe et al. 2018, Iwasato 2020, Modol, Bollmann et al. 2020, Nakazawa, Yoshimura et al. 2020, Nakazawa and Iwasato 2021) (Mizuno, Ikezoe et al. 2018). The pattern of patchwork-type spontaneous activity corresponds to the barrel map, therefore indicating the likelihood of this activity being crucial for the formation of a precise somatotopic map (Mizuno, Ikezoe et al. 2018, Nakazawa, Yoshimura et al. 2020). However, a paucity exists in our understanding of the source of the patchwork-type spontaneous activity. Some studies suggest that prior to the onset of exploratory whisker movement, sensory feedback from inadvertent whisker twitches is the source of spontaneous activity in the somatosensory cortex (Khazipov, Sirota et al. 2004, Tiriac, Uitermarkt et al.

2012, Akhmetshina, Nasretdinov et al. 2016, Dooley, Glanz et al. 2020). Contrary to this, recent work by our group demonstrated that only a small percentage (~11%) of patchwork-type spontaneous activity correlates with whisker twitches (Mizuno, Ikezoe et al. 2018). Hence, the major source of patchwork-type spontaneous activity remains unknown. Furthermore, to my knowledge, no study has elucidated whether the peripheral structure of the developing somatosensory system exhibits spontaneous activity itself, as is the case in visual and auditory systems.

Previous study by our lab revealed that the patchwork-type spontaneous activity observed in the neonatal mouse barrel cortex is blocked by the injection of a local anesthetic to the contralateral whisker pad but not by transection of the infraorbital nerve (ION) (Mizuno, Ikezoe et al. 2018), implying that the source is somewhere in the periphery but downstream of the ION. Based on these results, I postulated that the trigeminal ganglion (TG), which harbors the cell bodies of neurons that innervate the whisker pad, is the source of patchwork-type spontaneous activity in the somatosensory cortex. In the present study, I aim to elucidate whether the neonatal mouse TG exhibits spontaneous activity itself. To eliminate all inputs from the whisker pad while simultaneously preserving the cytoarchitecture of the TG, I established a novel *ex vivo* calcium imaging system to delineate the occurrence of spontaneous firing by neonatal TG neurons. With this method, I discovered that neurons in the whisker innervating area of the mouse TG generate spontaneous activity during the early postnatal period, but this activity largely diminishes by adulthood. The bulk of the spontaneously firing neurons in the neonatal stage have a medium-to-large diameter, which is a characteristic of the mechanosensory neurons. The spontaneous activity in

neonatal TG is sporadic, with no obvious spatiotemporal pattern or wide-scale co-activation of neurons. Nevertheless, a small population of neuron pairs, majorly located close to one another shows some evident correlation. The present study is the first to show that spontaneous activity is found in the peripheral structure of the somatosensory system during the neonatal stage.

RESULTS

Established *Ex vivo* imaging system for neonatal TG

Input from each whisker goes to TG, the principal trigeminal nucleus (PrV) in the brainstem, the ventral posteromedial nucleus (VPM) in the thalamus, and finally reaches barrel cortex layer 4, where each barrel receives input from a single whisker (**Figure 1a**). The TG has pseudo-unipolar sensory neurons whose processes innervate the periphery and brainstem. To identify the location of sensory neurons in the whole TG, I crossed the *Avil*-Cre mouse, which expresses Cre recombinase in peripheral sensory neurons, with the Rosa26-loxP-stop-loxP (LSL)-nuclear localization signal (nls) LacZ reporter (RNZ) mouse and obtained the *Avil*-Cre:RNZ mouse. X-Gal staining in the intact TG and DRG of this mouse at a neonatal stage revealed the distribution of sensory neurons along the dorsal surface of the TG (**Figure 1b**). The newly developed *Avil*-nlsRFP transgenic mouse (PB, TS, TI: unpublished) that expresses the red fluorescent protein (RFP) in the nuclei of peripheral sensory neurons also demonstrated the sensory neuron distribution in the TG (**Figure 1c-1d**).

Based on the innervation target of peripheral processes, the TG has three major branches: the ophthalmic branch (V1) that innervates the eye, the maxillary branch (V2) that innervates the whisker pad, and the mandibular branch (V3) that innervates the lower jaw. To identify the region of TG that houses neurons innervating the large whiskers, I placed DiI crystals around individual whisker follicles and observed the region of subsequent dye labeling. DiI applied around the A-row whisker follicles stained neurons whose cell bodies are on the anteromedial side of the dorsal surface of the TG (**Figure 1e**), and DiI application

around the E-row follicles stained neurons on the more lateral side (**Figure 1f**). These results demonstrate that a whisker-row-dependent topography exists along the dorsal surface of TG. On the other hand, when I placed DiI crystals around the follicles of C1 and C6 whiskers of different mice, no obvious difference in the localization of the labelled neurons was observed in the TG (**Supplementary Figure 1**), suggesting that the TG may not have a whisker-arc-dependent topography along its dorsal surface. I also placed DiI crystals in the lower jaw and observed subsequent labeling on the posterolateral side of the TG, implying that neurons in that region innervate the lower jaw (**Figure 1g**), which is consistent with previous reports (Erzurumlu and Jhaveri 1992, Laumonnerie, Bechara et al. 2015, Kitazawa and Rijli 2018). Hence, there exists an obvious topography in neuronal localization in the dorsal surface of TG depending on the projection sites of peripheral processes. Therefore, I identified the region of an intact TG that has neurons innervating the follicles of the large whiskers (**Figure 1h**).

To test my hypothesis that the whisker-innervating region of TG generates spontaneous activity during neonatal stages, it is crucial to monitor neuronal activity in the intact TG, which was transected from other parts of the ascending trigeminal pathway. Thus, I established an *ex vivo* imaging system for neonatal TG. I crossed the *Avil*-Cre mouse with the Rosa26-LSL-GCaMP6s reporter (R26-GCaMP6s) mouse to express the genetically encoded calcium indicator GCaMP6s in TG neurons (**Figure 1i**). The TG is a fragile organ, so I utilized the whole TG, still attached to the cranial base for *ex vivo* imaging, by simply transecting its peripheral and central branch points to limit damage to the organ and retain its cytoarchitecture and microenvironment (**Figure 1j**).

Spontaneous activity observed in neurons of the whisker-innervating region in neonatal TG

Using my *ex vivo* setup (**Figure 1j**), I performed calcium imaging in the whisker-innervating region of TG isolated from the *Avil*-Cre:R26-GCaMP6s mice at P4–P6. In my experimental design, to cover the entire whisker-innervating area of TG, three regions were imaged: locus 1 (L1), locus 2 (L2), and locus 3 (L3), following which the organ was perfused with high potassium buffer to confirm its viability (**Figure 2a**). I detected clear spontaneous activity in all of the L1, L2, and L3 regions at a cellular resolution (**Figures 2b-2d**). Most neurons fired infrequently and did not exhibit obvious oscillatory calcium transients (**Figures 2e-2f**). At the population level, the spontaneous activity exhibited no recognizable synchronization for most of the active neurons, thereby appearing random, both spatially and temporally. Thus, I detected spontaneous activity in neurons of neonatal TG's whisker-innervating region. Since this spontaneous activity occurred independent of whisker input, it originated within the TG itself.

To examine more systematically if spontaneous activity occurring in the neonatal TG was random or correlated, I placed regions of interest (ROIs) over all neurons that fired during the 10 min imaging session (Image 3) (**Figure 2g**). Next, I calculated the Pearson's correlation coefficient for fluorescent signal intensity between all the possible ROI pairs, which I then visualized with a color-coded correlation matrix (**Figures 2h and 2i**). No obvious cluster was identified, and only ~1.9% of ROI pairs showed correlated firing, where ROI pairs having a correlation coefficient >0.5 were considered to be correlated. To evaluate

if the correlated pairs of neurons are located close to one another, I calculated the distance between all the possible ROI pairs and compared it with their respective correlation coefficients (**Figure 2j**). I found that the distance between correlated ROI pairs (median:123 µm) was significantly smaller than the distance between non-correlated ROI pairs (median:199 µm), suggesting that correlated ROI pairs are majorly located closer to one another when compared with non-correlated ones (**Figure 2k**). Overall, it appears that the spontaneous activity in neonatal TG is spatiotemporally sparse, with a small number of neuron pairs exhibiting some evident correlation.

Age-dependent comparison of the spontaneous activity in TG

To compare spontaneous activity in TG across different stages of development, I considered four age groups: P0–P1 (newborn stage), P4–P6 (neonatal stage), P14–P16 (juvenile stage), and >P60 (adult stage), and performed *ex vivo* calcium imaging using *Avil*-Cre:R26-GCaMP6s mice (**Figures 2a and 3a**). The newborn stage was selected to elucidate if spontaneous activity in TG initiates before the formation of the barrel map; the juvenile stage was selected to determine if spontaneous activity continues in the second postnatal week, and the adult stage was selected to reveal whether or not TG spontaneous activity is specifically a characteristic of the early-postnatal period. At P0–P1, the TG exhibited clear spontaneous activity with ~50 neurons firing spontaneously in an imaging locus (660 µm x 660 µm) in a 5 min duration (Avg. of Images 1, 2, and 3), which was similar to the P4–P6 stage wherein ~40 neurons fired spontaneously in the same duration (**Figure 3b**). I also observed spontaneous activity in the P14–P16 stage with ~30 neurons firing spontaneously in a 5 min

duration (**Figure 3b**). Similar to the P4–P6 stage, in the P0–P1 and P14–P16 stages, no obvious pattern or correlated firing of a large group of neurons was identified, nor did the neurons seem to exhibit an oscillatory firing pattern. Contrary to the first two postnatal weeks, minimal to no spontaneous activity was observed in adult TG, with <5 neurons firing spontaneously in a 5 min duration (**Figure 3b**). I evaluated the viability of the TG by subjecting it to high potassium buffer (Image 4) after EVB (**Figure 2a**) and found that TG neurons in all stages reacted to high potassium irrespective of whether or not they fired spontaneously (**Supplementary Figure 2**), thereby confirming that the explant was viable and healthy. Consequently, despite the adult TG's viability, spontaneous activity was greatly reduced, indicating that it was a hallmark of that stage.

The TG evidently increased in size during development, as did the GCaMP$^+$ area (**Figure 3a**). Therefore, the total number of neurons in each imaging locus was likely to decline with age. To quantify this, I used the *Avil*-nlsRFP mouse. First, I calculated the area of the nlsRFP$^+$ region across the ages to see the factor by which it increases with development and found that it almost quadruples by the adult stage when compared with the P0–P1 stage (**Figure 3c; Supplementary Figure 3**). Next, I quantified the total number of nuclei (neurons) in L1, L2, and L3 across the stages of development (**Figure 3c**). Expectedly, the number of neurons in each locus significantly decreased with age, from >600 neurons/image in the P0–P1 stage, to 300-350 neurons/image in the P4–P6 and P14–P16 stages, and <200 neurons/image in the adult stage (Avg. of L1, L2, and L3) (**Figure 3d**). I calculated the percentage of neurons firing spontaneously across the stages of development by dividing the number of spontaneously firing neurons (**Figure 3b**) by the total number of neurons visible

in each imaging region (**Figure 3d**). My results revealed that in the P4–P6 stage, ~12% of neurons fire spontaneously, whereas in the adult stage, <2% of neurons fire spontaneously (**Figure 3e**), thereby confirming that spontaneous activity in TG neurons significantly diminishes by the adult stage.

Additionally, I compared the firing characteristics of spontaneous activity in TG neurons across development (**Figure 3f**). The amplitude of calcium transients significantly fluctuated across development (**Figure 3g**), as did the rise time of individual calcium transients across the first two postnatal weeks (**Figure 3h**). The decay time and total duration of individual calcium transients decreased across the first two postnatal weeks (**Figures 3i and 3j**). Furthermore, I found that by the adult stage, along with the decline in the total number of spontaneously firing neurons, their frequency of firing also decreases when compared with the first two postnatal weeks (**Figures 3f and 3k**).

To conclude, I found the existence of spontaneous activity in TG across the first two postnatal weeks, with subtle changes in their firing patterns across development, implying that spontaneous activity is evolving with age.

Neuronal subtypes firing spontaneously in neonatal TG

The rodent TG has three major sensory neuronal subtypes based on the diameter of the soma: small diameter (SD) is a characteristic of nociceptive neurons, and medium diameter (MD) to large diameter (LD) are characteristics of mechanosensory neurons. Previous studies in peripheral sensory neurons of adult mice claimed that the diameter of SD, MD and LD

neurons is <20 µm, 20-25 µm, and >25 µm, respectively (Kim, Anderson et al. 2016). To estimate the size of sensory neuron subtypes in neonatal TG, I used calcitonin gene-related peptide (CGRP) and neurofilament-200 (NF-200) as phenotypic markers to differentiate between SD-MD, and MD-LD neurons, respectively, and performed immunostaining in P6 TG sections (**Figures 4a and 4b**). My results showed that the diameter of $CGRP^+$ neurons and $NF\text{-}200^+$ neurons are 18.11 ± 4.26 µm and 26.36 ± 4.88 µm, respectively. My data demonstrating the distribution of neurons in neonatal TG based on their soma-diameter was similar to that shown in adult peripheral sensory neurons; thus, I used the same definition of SD (<20 µm), MD (20-25 µm), and LD (>25 µm) neurons as reported previously (**Figure 4c**) (Kim, Anderson et al. 2016).

I then quantified the total population of neurons in P4–P6 TG based on their soma size. To activate the majority of the sensory neurons, I subjected the *Avil*-Cre:R26-GCaMP6s mouse TG to high potassium buffer *ex vivo* (Image4 (I4)) (**Figure 2a**). Then, I measured the diameter of each neuron in an imaging locus (L3) in which the soma boundary was clearly visible (**Figure 4d**). I found that 67.3%, 27.3%, and 5.5% of neurons are SD, MD and LD neurons, respectively (**Figures 4e and 4h**) (n= 220 neurons, 2 animals). This was similar to previous reports in adult rat TG which suggest that >90% of neurons are SD-MD neurons (Ambalavanar and Morris 1992, Lennerz, Rühle et al. 2008, Messlinger and Russo 2019). Next, I chose neurons that fired spontaneously in a 10 min duration (Image3 (I3)) (See Figure 2a) and whose soma-boundary was clearly visible to measure their respective diameters (**Figure 4f**). I found that 17.1%, 39.5%, and 43.4% were SD, MD, and LD neurons, respectively (**Figure 4g and 4h**). It is important to note that 82.9% of spontaneously firing

neurons were MD-LD neurons, the majority of which are likely to be mechanosensory neurons (**Figure 4h**) (n= 76 neurons, two animals).

Since ~12.3% of P4–P6 neurons fired spontaneously in a duration of 5 min (**Figure 3e**), I calculated the active proportion in each neuronal subtype population and roughly estimated that 3% (≒12.3x17.1/67.3), 18% (≒12.3x39.5/27.3), and 98% (≒12.3x43.4/5.5) of SD, MD, and LD neurons, respectively, fired spontaneously in a duration of 5 min. Hence, the majority of LD neurons and a negligible fraction of SD neurons fire spontaneously in neonatal TG *ex vivo*.

Importance of extracellular calcium in generating spontaneous activity in neonatal TG

To elucidate the mechanism generating spontaneous activity in P4–P6 TG, I primarily focused on purinergic receptors as potential candidates since these molecules are known to play a key role in the generation of spontaneous activity in developing mouse cochlea (Tritsch, Yi et al. 2007, Babola, Kersbergen et al. 2020). My RNA-seq data for P5 TG revealed that *P2RX3* gene has the highest expression among all the purinergic receptor genes expressed (**Supplementary Figure 4a; Table 1**). My quantitative reverse transcription-PCR (qRT-PCR) confirmed that *P2RX3* gene is highly expressed in the TG but not in the brain at P5 (**Supplementary Figure 4b**). To test if *P2RX3* plays a role in generating spontaneous activity in neonatal TG, I generated *P2RX3* knockout mice using CRISPR/Cas9 (**Supplementary Figure 5**). Then I performed *ex vivo* calcium imaging in P4–P6 TG of

P2RX3 knockout mice that express GCaMP6s in the TG neurons (*Avil*-Cre: R26-GCaMP6s: *P2RX3*$^{-/-}$ mice). However, contrary to our expectation, I observed clear spontaneous activity (n= 3) **(Figure 5a**). Parallelly, to widen my scope from *P2RX3* to all the purinergic receptors expressed, I tested their broad pharmacological inhibitors (Suramin and PPADS) for the TG prepared from wild-type mice by using our *ex vivo* imaging system (**Figure 5b**). These too did not have any obvious effect on perturbing spontaneous activity in neonatal TG (**Figure 5c**). These results indicate that *P2RX3* is not essential for the generation of spontaneous activity in the neonatal TG. I next tested the broad inhibitors of ionotropic glutamate receptors (DNQX+ APV), cholinergic receptors (Atropine), glycinergic receptors (Strychnine), and GABA receptors (Gabazine) in TG *ex vivo* since each of these is known to be involved in the generation of spontaneous activity in other developing systems such as retinal ganglion cells, spinal cord, hippocampus, etc. (Wong, Meister et al. 1993, Aguayo, van Zundert et al. 2004, Blankenship, Ford et al. 2009, Scain, Le Corronc et al. 2010, Ford, Félix et al. 2012, Maccione, Hennig et al. 2014, Martini, Guillamón-Vivancos et al. 2021). Nevertheless, none of these perturbed or inhibited the spontaneous activity in neonatal TG (**Figures 5d to 5f**). Thus, these neurotransmitter receptors had no obvious effect on spontaneous activity in neonatal TG.

Lastly, I wanted to delineate the role of extracellular calcium in generating spontaneous activity in the TG. I tested the calcium chelator (EGTA) in calcium-free EVB (0 Ca^{2+} EVB), and found that it almost completely blocked spontaneous activity in P4–P6 TG of *Avil*-Cre:R26-GCaMP6s mice (n= 3) (**Figures 5g and 5h**). After washing it out, the organ reacted robustly to high potassium buffer, indicating that the TG was still viable. This

result indicates that extracellular calcium plays a crucial role in generating spontaneous activity in neonatal TG.

DISCUSSION

The present study provides the first evidence of the occurrence of spontaneous activity in the peripheral structures of the somatosensory system during the early postnatal period. Spontaneous activity in the developing sensory systems is important for the refinement of neural circuits. By establishing a method of *ex vivo* calcium imaging, I discovered that neurons of the TG that transmit tactile sensation from the whiskers to the brainstem exhibit spontaneous activity during the first postnatal week (**Figures 1 and 2**). This activity is largely sporadic, with no obvious spatiotemporal pattern or wide-scale co-activation of neurons (**Figures 2 and 3**). Even so, a small population of neuronal pairs, which tend to localize close to each other, shows some evident correlation. Spontaneous activity in the TG is also observed during the second postnatal week but majorly diminishes by adulthood (**Figure 3**). Additionally, the majority of the spontaneously firing neurons have a medium-to-large diameter, which is a characteristic of mechanosensory neurons (**Figure 4**). Furthermore, this activity is blocked by chelation of extracellular calcium and, in accordance with my pharmacological study data, it may originate in a cell-intrinsic manner (**Figure 5**).

Spontaneous activity in the somatosensory periphery during the neonatal stage

Spontaneous activity in the developing nervous system has been well studied in the peripheral structures of the visual and auditory systems. In the visual system, synchronous bursts are observed in the retinal ganglion cells of isolated neonatal retinas, which propagate

tangentially across the organ in a wave-like manner (Galli and Maffei 1988, Meister, Wong et al. 1991, Wong, Meister et al. 1993, Wong, Chernjavsky et al. 1995). Similarly, in the auditory system, spontaneous activity is observed in the spiral ganglion cells and inner hair cells from the isolated neonatal cochlea (Walsh and McGee 1987, Lippe 1994, Glowatzki and Fuchs 2002, Jones, Leake et al. 2007, Tritsch, Yi et al. 2007, Johnson, Eckrich et al. 2011). In the visual system, the spontaneous activity in the immature retina is transmitted to the visual cortex and superior colliculus, wherein, the wave-like pattern is also preserved (Ackman, Burbridge et al. 2012, Siegel, Heimel et al. 2012). Similarly, in the auditory system, the spontaneous activity in the developing cochlea is transmitted to the auditory cortex and inferior colliculus, wherein the activity is observed in accordance with the future tonotopic axis (Babola, Li et al. 2018). During the first postnatal week, neurons in barrel cortex L4 exhibit correlated spontaneous activity, where neurons within the same barrel tend to fire together, giving a patchwork-like appearance (Golshani, Gonçalves et al. 2009, Yang, Hanganu-Opatz et al. 2009, Yang, An et al. 2013, Mizuno, Ikezoe et al. 2018, Iwasato 2020, Modol, Bollmann et al. 2020, Nakazawa, Yoshimura et al. 2020, Nakazawa and Iwasato 2021). Along with L4 neurons, the thalamocortical axons also exhibit patchwork-type spontaneous activity in the barrel cortex L4 in neonates (Mizuno, Ikezoe et al. 2018).

My current discovery of spontaneous activity in the whisker-innervating neurons of the neonatal TG (**Figures 1 and 2**) underscores the likelihood of it being the source of spontaneous activity in the cortex. Since I used a TG transected from all upstream afferents and inputs, it clearly indicates that the spontaneous activity observed in TG neurons originates within the organ itself (**Figures 1 and 2**). Furthermore, I found that more than 80%

of the spontaneously firing neurons are medium-to-large-diameter neurons, which are likely the mechanosensory neurons (**Figure 4**). Mechanosensory neurons play a pivotal role in transmitting and processing tactile information from individual whiskers to the barrel cortex. Thus, spontaneous activity in these neurons during the early postnatal period may aid in the refinement of the ascending somatosensory pathway which in turn leads to precise sensory processing in the later stages.

I further found that the spontaneous activity in the TG is a likely characteristic of the early postnatal period since it was majorly diminished by the adult stage, wherein only a small population (<2%) of neurons fired spontaneously (**Figure 3**). On the other hand, it was somewhat unexpected to observe spontaneous activity in the TG neurons during the second postnatal week, because the cortical spontaneous activity no longer arrives via thalamocortical axons by that age (Nakazawa, Mizuno et al. 2018). However, this was consistent with the visual and auditory systems, where the peripheral structures exhibit spontaneous activity even during the second postnatal week (Wong 1999, Tritsch, Yi et al. 2007, Ford, Félix et al. 2012). In the mouse visual system, the retinal spontaneous activity observed during the second postnatal week is transmitted to the thalamus and superior colliculus but not to the cortex (Gribizis, Ge et al. 2019). By the second postnatal week, the majority of inputs to the cortex become cortico-cortical, as opposed to the majority of inputs being thalamo-cortical during the first postnatal week (Micheva and Beaulieu 1996, Bureau, von Saint Paul et al. 2007, Piñon, Jethwa et al. 2009, Marques-Smith, Lyngholm et al. 2016, Valiullina, Akhmetshina et al. 2016). Hence, it is likely that although the TG continues to

exhibit spontaneous activity by the P14–P16 stage, it is no longer a source of the cortical spontaneous activity by that stage.

The thalamus and whisker pads have also been candidates as probable sources for the spontaneous activity observed in the neonatal barrel cortex. In the thalamocortical slice prepared from prenatal mouse, wave-type spontaneous activity originates in the thalamus (Moreno-Juan et al., 2017, Anton-Balanos, et al., 2019). Nonetheless, injection of a local anesthetic to the contralateral whisker pad in the neonatal mouse blocks the cortical spontaneous activity (Mizuno, Ikezoe et al. 2018). This result suggests that, at least in the neonatal stage, the source is most likely in the periphery itself, thereby excluding the brainstem and thalamus as possibilities. On the other hand, the TG has pseudo-unipolar sensory neurons whose peripheral afferents innervate the whisker pad, which explains how it can be silenced by a local anesthetic. Sensory feedback from inadvertent motor activity in the periphery, such as self-generated spontaneous whisker movements, are also suggested to induce spontaneous activity in the developing barrel cortex and thalamus before the onset of exploratory whisker movement (Khazipov, Sirota et al. 2004, Tiriac, Uitermarkt et al. 2012, Akhmetshina, Nasretdinov et al. 2016, Dooley, Glanz et al. 2020). However, in our previous study, the majority (89%) of patchwork-type activity in the neonatal barrel cortex L4 was not associated with corresponding whisker movements (Mizuno, Ikezoe et al. 2018). In addition, transection of the ION did not block the cortical L4 spontaneous activity (Mizuno, Ikezoe et al. 2018), suggesting that a major source is likely to be downstream of the ION. In the present study, by establishing a novel *ex vivo* imaging system, I demonstrated the presence of

spontaneous activity in the neonatal TG, which is likely a major source of the spontaneous activity that is observed in the neonatal barrel cortex.

How does the patchwork-type pattern of cortical spontaneous activity emerge?

If the TG is the source of cortical spontaneous activity, where and how does the patchwork-type pattern emerge? I did not identify any obvious pattern or wide-scale co-activation of a large group of neurons in the neonatal TG (**Figure 2**). Still, I was able to find a small population of neuronal pairs, that tend to be located close to each other and exhibit some evident correlation. These neurons may possibly innervate the same whisker follicles. In the TG, there exists a whisker-row-dependent spatial topography in neuronal soma localization (**Figure 1**); yet, there is no obvious morphological clustering for the group of neurons that innervate the same whisker (Erzurumlu and Jhaveri 1992, Da Silva, Hasegawa et al. 2011, Laumonnerie, Bechara et al. 2015, Kitazawa and Rijli 2018). Therefore, it is still possible that the neurons that innervate the same whisker follicle tend to fire together, and in this scenario, the TG should already have a template for the patchwork-type pattern that gets transmitted to the cortex via the brainstem and thalamus. Another possibility is that the spontaneous activation of a single TG neuron further activates multiple brainstem neurons within the same barrelette, which subsequently activates a single barreloid in the thalamus. Thus, the activity from one TG neuron may amplify at each relay station to ultimately activate multiple neurons within the same barrel, thereby forming a “patch”, and hence revealing the

patchwork-like pattern observed in the cortex. In this scenario, the spontaneous activity originates from the TG, but the patchwork-type pattern shapes in the brainstem. A recent study by our group demonstrated that transection of ION at P0–P1 disrupts the pattern of cortical spontaneous activity observed at P5 (Nakazawa, Mizuno et al. 2018). Therefore, in either of the scenarios discussed above, the template of the patchwork-type pattern should be generated depending on the inputs from the whiskers in the newborn stage, such as P0–P1.

Mechanism generating spontaneous activity in TG

In the developing rodent retina, spontaneous activity has three sequential stages, each with its own mechanism: stage I waves (E16-P0) are inhibited by blockers of gap junctions and adenosine receptors, stage II waves (P0-P9) are inhibited by blockers of acetylcholine and GABA receptors, and stage III waves (P10-P14) are inhibited by blockers of glutamate and muscarinic receptors (Feller, Wellis et al. 1996, Syed, Lee et al. 2004, Zheng, Lee et al. 2004, Maccione, Hennig et al. 2014). In the developing cochlea, spontaneous activity is inhibited by blockers of purinergic receptors (Tritsch, Yi et al. 2007, Babola, Li et al. 2021). Unlike the retina and cochlea, the isolated TG does not have synapses. Hence, it is unlikely for neurotransmitters to play a role in generating spontaneous activity. This is validated by our findings in this study demonstrating that the spontaneous activity in TG is not inhibited/ perturbed by pharmacological blockers of glutamatergic receptors, cholinergic receptors, GABA-A receptors, and glycinergic receptors, and purinergic receptors (**Figure 5**). I assume

that the spontaneous activity in TG might be generated in a cell-intrinsic manner. The surge in intracellular Ca^{2+} during spontaneous Ca^{2+} transients is either due to the influx of extracellular Ca^{2+}, or due to release of Ca^{2+} from intracellular stores. I found that chelation of extracellular Ca^{2+} with EGTA blocked the TG spontaneous activity (**Figure 5**). On the same note, a previous electrophysiological study demonstrated that induced action potentials in neonatal TG neurons were highly sensitive to reductions in extracellular calcium *in vitro* (Cabanes, Armentia et al. 2002). Thus, extracellular Ca^{2+} plays a crucial role in the generation of neonatal TG spontaneous activity (**Figure 5**). Among the 5 given sub-classes of calcium channels (HGNC classification), only the voltage-gated calcium channels (VGCCs) can cause the extracellular calcium to affect the spontaneous activation of the cells (**Table 2**). Thus, it is likely that the influx of extracellular calcium via the VGCCs activated by spontaneous fluctuation in membrane potential generates spontaneous activity in P4-P6 TG.

In summary, I discovered spontaneous activity in the sensory neurons located in the whisker-innervating region of neonatal TG *ex vivo*, which is the first evidence of spontaneous activity in the peripheral structure of the developing somatosensory system. Our findings will help further our understanding of the role of spontaneous activity in the development and establishment of precise and mature sensory circuits.

MATERIALS AND METHODS

Animals

All experiments were performed according to the guidelines for animal experimentation of the National Institute of Genetics (NIG) and were approved by the animal experimentation committee of the NIG. Sex of pups was not identified. PCR primers used for genotyping of *Avil*-Cre (RBRC10246) (Zhou, Wang et al. 2010, Da Silva, Hasegawa et al. 2011), Rosa26-LSL-nls-lacZ (RNZ) (RBRC02657) (Kobayashi, Sano et al. 2013), R26-LSL-GCaMP6s (R26-GcaMP6s) (Ai96: 024106) (Madisen, Garner et al. 2015), and *Avil*-nlsRFP (PB, TS, TI: unpublished) mice were KS149/KS150, KS109/KS110 and KS149/KS150, respectively (**Table 3**).

Generation of *P2RX3* knockout mouse

P2RX3 global knockout mice were generated using the CRISPR/Cas9 system (Ran, Hsu et al. 2013, Hashimoto and Takemoto 2015). To delete the putative promoter, translational initiation site, and translational initiation site of the *P2RX3* gene, single guide RNAs (sgRNAs) were designed flanking exon 1 of the *P2RX3* gene using the CRISPRdirect (Naito, Hino et al. 2014) and CRISPOR (Concordet and Haeussler 2018) tools. sgRNAs were selected based on high MIT and CFD score (>90), low off-target mismatches, and their location with respect to exon 1. Based on these criteria, two sgRNAs were selected (sgRNA_62Forw, sgRNA_1228Forw) (**Table 3**). Alt-R CRISPR-Cas9 crRNAs and Alt-R CRISPR-Cas9 tracrRNA were ordered from IDT (Integrated DNA Technologies). The

annealed scRNAs and tracrRNA, and TrueCut Cas9 protein v2 (Invitrogen) were premixed and electroporated into fertilized eggs of B6/C3H F2 using CUY21EDIT II electroporator and LF501PT1-10 platinum plate electrode (BEX Co. Ltd.). Founder mice were screened by genotyping using primers KS253/254 and OP31/OP32 (**Table 3**). Sequences of the four founder mice were determined to assess the deletion.

RT-PCR was used to confirm the absence of *P2RX3* transcripts in *P2RX3*$^{-/-}$ (KO) mouse. TGs were carefully isolated from P4–P6 *P2RX3*$^{-/-}$ (KO) and *P2RX3*$^{+/+}$ (WT) littermates on ice, and immediately transferred to ice-cold RNALater solution (Sigma) in which they were incubated at room temperature for up to one week. RNA was isolated using the RNEasy Mini Kit (Qiagen, #74104) and stored in -80^{o}C. cDNA was synthesized using the PrimeScript RT reagent kit (Takara, #RR037Q), and was used as templates for RT-PCR. Primer pairs OP11/OP12 and OP19/OP20 were used for *GAPDH* and *P2RX3*, respectively. The sequence for all the primers is mentioned in Table 3.

X-Gal staining

Male *Avil*-Cre mice were mated with female RNZ mice to obtain *Avil*-Cre:RNZ mice. *Avil*-Cre:RNZ pups were sampled at P4–P6, and the TG was isolated while still attached to the cranial base by specifically transecting its peripheral and central nerve terminals. Post-dissection, the whole TG was fixed in 4% paraformaldehyde (PFA) in 0.1 M phosphate buffer (PB) for 2 hours at room temperature, and rinsed thrice with 0.05 M PB. The TG was stained overnight at 37^{o}C with X-Gal staining solution (5 mM potassium ferricyanide, 5 mM potassium ferrocyanide, 2 mM magnesium chloride, 1mg/ml X-Gal in 0.05 M PB). The

following day, the TG was rinsed thrice with 0.05 M PB and post-fixed in 4%PFA in 0.1 M PB overnight. Images were acquired using the M205 FCA microscope (Leica) and DFC7000T camera (Leica).

DiI labelling

DiI crystals (Invitrogen, D282) were placed around individual whisker follicles of P0–P1 mice using a 35G beveled needle (World Precision Instruments, NF35BV-2), following which, the pups were warmed on a heating pad (37^{o}C) for 10-15 min before returning to the mother. Four to five days later, the pups were sampled, and the TG was carefully isolated while still attached to the cranial base. DiI labelling was observed in the TG and images were acquired using the M205 FCA microscope (Leica) and DFC7000T camera (Leica).

Immunohistochemistry

Mice were anesthetized with pentobarbital intraperitoneal injection and perfused with 0.9% NaCl followed by 4% paraformaldehyde (PFA) in PB for fixation. The TG was isolated while still attached to the cranial base and post-fixed overnight in 4% PFA in 0.1 M PB at 4^{o}C. The following day, isolated TGs were washed with 0.1 M PB and transferred to 30% sucrose in 0.1 M PB at 4^{o}C till sectioning. For sectioning, TGs were carefully separated from the cranial base and fixed in OCT compound. 20 µm-thick longitudinal sections were made using a cryostat (Leica CM3050S) and mounted on MAS-coated slides (Matsunami, MAS-02). The slides were dried overnight at RT and immunostaining was performed. Slides were incubated

in blocking buffer (3% goat serum, 0.5% TritonX-100 in phosphate buffer saline (PBS)) for 2 hours at RT, following which, primary antibody solution was applied: CGRP (1:1000, Immunostar #24112), NF-200 (1:500, Sigma #N4142), NeuN (1:1000, Millipore). The slides were incubated overnight on a shaker at 4^{o}C. The following day, the slides were washed with 1X PBS and incubated in secondary antibody solution: Alexa 488 (Goat anti-rabbit IgG, Invitrogen #A11034) for 1 hour on a shaker at RT. After this, the slides were washed with 1X PBS and incubated in DAPI solution (1 ug/ml) for 2 min at RT. The slides were again washed with 1X PBS and mounting medium was applied followed by coverslip. The slides were incubated at 4^{o}C overnight and sealed the following day. Images were taken using a confocal microscope (Leica TCS SP5 II) and 10x and 40X lens. Cell Count and measurement of soma diameter for individual cells were performed using Fiji ImageJ.

Ex vivo calcium imaging of TG

The male *Avil*-Cre mice were mated with the female R26-GcaMP6s mouse to obtain *Avil*-Cre:R26-GcaMP6s pups. *Ex vivo* buffer (EVB) (pH 7.4) contained 135 mM NaCl, 5 mM KCl, 1.5 mM $CaCl_2$, 1.5 mM $MgCl_2$, 20 mM HEPES (pH 7.4) and 10 mM Glucose. High potassium buffer (pH 7.4) contained 90 mM NaCl, 50 mM KCl, 1.5 mM $CaCl_2$, 1.5 mM $MgCl_2$, 20 mM HEPES (pH 7.4) and 10 mM Glucose (Hirata, Kumada et al. 2012). Intact TGs attached to the cranial base were carefully isolated on ice-cold EVB from *Avil*-Cre:R26-GcaMP6s mice at different stages of development (P0–P1, P4–P6, P14–P16, >P60). Following dissection, the cranial base was affixed to the detachable base of the imaging chamber using superglue. Henceforth, the organ was continuously perfused with EVB,

followed by high potassium buffer (10-15 min). The buffers were bubbled with 95% O_2 and 5% CO_2. For pharmacological studies, EVB was perfused for 25 min, then one or two of the following drugs was perfused for 20 min: PPADS (100 µM, Tocris), Suramin (500 µM, Sigma), DNQX (100 µM, Sigma), D-APV (50 µM, Abcam), Gabazine (100 µM, Abcam), Atropine (15 µM, Sigma), Strychnine (5 µM, Abcam), EGTA (50 mM, Sigma). Thereafter, the drug was washed away by perfusion with EVB for 20-30 min, following which high potassium buffer was perfused for 10 min to evaluate organ viability. All the buffers were maintained at a stable temperature of 25^{o}C and perfused at a rate of ~2 ml/min. Time lapse images were acquired at 1 Hz frequency using an upright microscope (Olympus, BX61), a monochromatic sCMOS camera (TELEDYNE Photometrics, Prime BSI) and a 20x water immersion lens (Olympus). All TGs were used within 3 hours of dissection.

Ex vivo calcium image analysis and quantification

Preprocessing

To analyze the firing pattern of individual cells, I bleach-corrected (Bleach correction plugin) and motion-corrected (Turbo-Reg plugin) the time-lapse images using Fiji/ImageJ version 1.53f, to minimize the effect of photobleaching and fix the inadvertent small movements during image acquisition. Slices with large fluctuations were removed from analyses.

Region of Interest (ROI) Detection

To detect spontaneously active neurons in a unbiased manner when comparing between the different age-groups (**Figure 3**), I used the EZcalcium toolbox of MATLAB (Cantu, Wang et al. 2020), which uses the algorithm CaImAn (Giovannucci, Friedrich et al. 2019) for automated ROI detection. I used the following settings for ROI detection with CaImAn: initialization (Greedy), search method (Ellipse), deconvolution (Constrained foofsis SPGL1), autoregression (Decay), merge threshold (0.95), fudge factor (0.95), spatial downsampling (1), temporal downsampling (1), temporal iteration (5). If some ROI was not detected by the software, it was added manually. For all the detected ROIs, a MATLAB data file was generated which contained the extracted fluorescence (dF/F) for each ROI along with a contour plot displaying their individual shape and location. Next, using the ROI refinement module of the EZcalcium toolbox, I manually inspected the individual traces and shapes of each of the ROIs to exclude the false positives (such as low activity or incomplete peaks). A contour plot was generated for the refined set of ROIs. For generating the potassium plots (Supplementary Figure 2), 15 random ROIs from each of the four stages of development were manually selected using Fiji/Image J. Their fluorescent intensities were also calculated using Fiji/Image J and further calculations were performed in Microsoft Excel.

Peak Detection and Characterization

All the ROIs detected and refined using the EZcalcium toolbox were further analyzed using the PeakCaller script written in MATLAB (Artimovich, Jackson et al. 2017) to characterize peaks of the calcium transients in details. The script was modified to calculate the peak parameters from raw data instead of the detrended data. The raw data was smoothed using

the Savitzky-Golay filter to remove the effect of background fluctuations. Peak parameters were automatically calculated based on the given settings: required rise % (20), required fall % (15), maximum lookback (30), maximum lookahead (25). The exponential moving average (2-sided) option was selected for calculating the underlying trendline. dF/F threshold was taken as mean + standard deviation. Based on these settings, individual peaks for each ROI were detected. ROIs with no detectable peaks were manually excluded from analysis. The script calculated the amplitude, rise time, decay time and total duration of each peak. It also generated raster plots (**Figure 3f**) to summarize peak properties from all the detected ROIs. Any false positives were manually removed from analysis using Microsoft Excel. For generating the potassium plots (Supplementary Figure 2), calculations were done using Microsoft Excel. Sliding window F_o was taken as the average fluorescent intensity across 60 frames, and dF/F_o defined as $(F_t-F_o)/F_o$ was calculated accordingly. Firing threshold was taken as 10*SEM. A binary heatmap was generated where $dF/F_o >=$ threshold was taken as 1, and $dF/F_o <$ threshold was taken as 0. In accordance with the schematic shown in Figure 2a, quantitative analysis was done as follows: from Images 1, 2, and 3 for Figures 3b, 3d and 3e; Images 1 and 2 for Figures 3g to 3k; from Image 3 for Figures 2g to 2k and Figures 4f to 4h; from Image 4 for Figures 4d to 4e, 4h.

Correlation Analysis

For correlation analysis (**Figures 2g to 2k**), ROIs were manually selected from all the detected spontaneously firing neurons in a 10 min duration (Image 3) using Fiji/ImageJ. Their fluorescent intensities were imported from Fiji/Image J and further calculations were done

on Microsoft Excel. Sliding window F_o was taken as the average fluorescent intensity across 60 frames, and dF/F_o was calculated accordingly. The firing threshold was taken as Mean + standard deviation and only the transients exceeding this threshold were used for further analysis. One firing event was considered as the period of time from which dF/F_o>threshold to when dF/F_o<threshold. For all the ROI pairs, Pearson's correlation coefficient was calculated using Prism GraphPad. A correlation matrix was constructed, and hierarchal clustering was performed using R studio. For all the ROI pairs having high correlation (correlation coefficient >0.5), their individual calcium traces were manually compared to validate the analysis method.

The coordinates for all ROIs were exported from Fiji/Image J, and the distance between all the possible ROI pairs were calculated on Microsoft Excel using the following formula: Distance between two ROIs = $\sqrt{(x2-x1)^2 + (y2-y1)^2}$, where x1, y1 and x2, y2 are respective the coordinates of the two ROIs.

Image Analysis of *Avil*-nlsRFP mouse

Intact TGs attached to cranial base were isolated from the *Avil*-nlsRFP Tg3 mouse (PB, TS, TI, unpublished) at different stages of development (P0–P1, P4–P6, P14–P16, >P60). Following dissection, the cranial base was affixed to the detachable base of the imaging chamber using superglue. Henceforth, the organ was continuously perfused with EVB. For counting the total number of neuronal nuclei visible in each frame (**Figures 3c and 3d**), images were taken with an upright microscope (Olympus, BX61), a monochromatic sCMOS

camera (TELEDYNE Photometrics, Prime BSI) and a 20x water immersion lens (Olympus). Image analysis was performed using Fiji/ImageJ. Firstly, the background was subtracted (100) and the image was made binary. Then, it was converted to a mask and the watershed function was applied. Lastly, the particle size was analyzed to count the total number of neuronal nuclei. Low magnification images were acquired using the M205 FCA microscope (Leica) and DFC7000T camera (Leica).

Temporal color-coding maps

For the pharmacological inhibitor experiments (**Figure 5**), temporal color-coding maps were generated using Fiji/Image J. Firstly, the time-lapse image was bleach corrected and registered. Then a F_o image was created by taking the average of all the images in the stacks. This F_o image was subtracted from each of the individual images in the stack to produce an F- F_o time-lapse, and a gaussian filter was applied. This processed dF/ F_o time lapse was used for making the temporal color-coding maps.

RNA Sequencing and Analysis

RNA isolation and library construction

TGs were carefully isolated from P5 and P15 C57BL/6J mice on ice, and immediately transferred to ice-cold RNALater solution (Sigma) in which they were incubated at room temperature overnight. Next day, they were transferred to 4^{o}C where they were stored for up to 1 week. RNA was isolated using the RNEasy Mini Kit (Qiagen, #74104) and stored in -

80^{o}C. Quality of the isolated RNA was assessed with the 2100 Bioanalyzer using the RNA 6000 nano kit (Agilent Technologies), and only the samples having RNA integrity number (RIN) >8 were used further. RNA seq library preparation was performed using the TruSeq stranded mRNA sample preparation kit (Illumina). The quantity and quality of the library was assessed using the Qubit BR kit (Invitrogen) and Bioanalyzer DNA 1000 kit, respectively (Agilent Technologies).

Sequence alignment and analysis

Paired end sequencing was performed using the HiSeq 2500 (Illumina) at a depth of 24 million reads/sample. The quality control for the sequence reads was conducted by the Trimmomatic (Bolger, Lohse et al. 2014). After trimming the adaptor sequences, I excluded the reads having the average base quality score < 25. The low-quality bases (base quality < 20) at the head and tail of each read were trimmed. I excluded the reads if the lengths of the reads were < 50 after the trimming. Then, the processed reads were aligned to the mouse genome (mm 10) using GSNAP (Wu and Nacu 2010). The sequence alignment map (SAM) files were converted to the binary alignment map (BAM) files by using the SAMtools (Li, Handsaker et al. 2009). The number of reads aligning to each gene were counted using featureCount (Liao, Smyth et al. 2014), and the raw expression counts were converted to counts per million (CPM). After adding the offset of 1, the CPM values were converted to the log-2 scale. The Limma/voom pipeline was used to detect differentially expressed genes between P5 TG and P15 TG (Law, Chen et al. 2014). Statistical significance was assessed by False discovery rate (FDR).

Quantitative RT-PCR

The RNA samples that were used for RNA sequencing were also utilized for performing quantitative RT-PCR (qRT-PCR). cDNA was synthesized using the PrimeScript RT reagent kit (Takara, #RR037Q), and was used as templates for qRT-PCR in 1:100 dilution. 2X SYBR Green (Applied Biosystems, #4367669) was used for the enzymatic reaction and real-time PCR was performed (Takara thermocycler: TP970 and TP850). Primer pairs OP11/OP12, OP19/OP20, and OP29/OP30 were used for *GAPDH*, *P2RX3*, and *Avil*, respectively. The sequence for all the primers is mentioned in Supplementary Table 3. Each sample had 2 biological replicates and 2 technical replicates.

Statistical Analysis and Computing

Fiji/ImageJ ver. 1.53f51 (Schindelin, Arganda-Carreras et al. 2012), MATLAB (2021) with Image Processing, Parallel Computing, Signal Processing, and Statistics and Machine Learning toolboxes (Mathworks), Microsoft Excel, Rstudio version 2021.09.2, and Prism GraphPad version 9.3.1 were used for data analysis and visualization. Unless otherwise mentioned, data are presented as mean ± standard error of mean (SEM). Statistical analyses were performed using Prism GraphPad. Shapiro-Wilk test was performed to check for data normality. p value<0.05 was considered significant. The asterisks in the figures indicate as follows: * for p<0.05, ** for p< 0.005, *** for p<0.001, and **** for p<0.0001. For the violin plot (Figure 2k), the middle dashed horizontal line represents the median, and the two

dotted horizontal lines represent the quartiles. Sample size for all the results is described in the figure legends.

Data Availability

The RNA sequencing datasets generated and analyzed during the current study are available in the DNA Data Bank of Japan (DDBJ) repository (PRJDB13784). The codes used for analysis and the data that support the findings are available (P.B., T.I.) upon reasonable request.

PUBLICATION DETAILS:

The majority of work in this thesis has been published in Scientific Reports (Banerjee et al., 2022).

Title: Spontaneous Activity in Whisker-Innervating Region of Neonatal Mouse Trigeminal Ganglion

Authors: P. Banerjee, F. Kubo, H. Nakaoka, R. Ajima, T. Sato, T. Hirata, T. Iwasato

Author contributions:

P.B. along with T.I conceived the study, designed the approach and experiments, and wrote the manuscript for publication with inputs from other co-authors. T.I. supervised and guided with all the steps of the overall project.

P.B. under the guidance of T.H established the *ex vivo* calcium imaging system and conducted all the relevant *ex vivo* experiments.

P.B. along with F.K. designed the pipeline to analyze the *ex vivo* calcium imaging data. The MATLAB script for the analyses was written by F.K., and the analyses was performed by P.B. under F.K.'s guidance.

P.B. prepared the tissue and isolated the RNA for RNA sequencing. The isolated RNA was handed over to H.N., who took care of the further steps till RNA sequencing and initial data processing. H.N. provided the differentially expressed genes list to P.B. ,who did further analyses on the same. The RNA-sequencing data was submitted to the DDBJ repository by H.N.

P.B. along with T.S. generated and maintained the *Avil*-nlsRFP mouse lines. P.B. performed the experiments and analysis on this transgenic mouse which are included in this thesis.

R.A. guided P.B. on generating a global knockout mouse using the CRISPR/Cas9 system. P.B. designed the guide RNAs and primers to generate the *P2RX3* knockout mouse, and performed further experiments and analysis on the same.

P.B. performed the remaining experiments and analysis included in this thesis.

ACKNOWLEDGEMENTS:

I take this opportunity to acknowledge and express my deepest gratitude towards Dr. Takuji Iwasato (Supervisor), NIG for giving me an opportunity to work under his expertise, for mentoring me at every step of the way, and for being exceptionally kind and patient with me throughout this journey. I am truly indebted and grateful.

I am extremely thankful to Dr. Tatsumi Hirata for guiding me with establishing the *ex vivo* imaging system, Dr. Fumi Kubo for helping me with the analysis of *ex vivo* calcium imaging data, Dr. Hirofumi Nakaoka for his invaluable help in performing RNA-sequencing and its data analysis, and Dr. Rieko Ajima for guiding me on generating a knockout mouse using the CRISPR/Cas9 system. I am especially thankful to Mr. Takuya Sato for kindly teaching me perfusion experiments, mouse handling, for helping me generate and analyze the *Avil*-nlsRFP transgenic mouse, and for a lot of other miscellaneous help. I am very thankful to Dr. Ramasamy Kandasamy for teaching me RNA isolation and guiding me with RNA Seq analysis. I would also like to express my deep gratitude towards Ms. Satoko Kouyama and Ms. Minako Kanbayashi for helping me maintain my mouse colonies.

I am very thankful to Dr. Hidenobu Mizuno, Dr. Shingo Nakazawa, Dr. Ramasamy Kandasamy and Dr. Naoki Nakagawa for helping me with my project with regular insights and fruitful discussions. I am grateful to my lab peers: Ms. Luwei Wang, Ms. Chiemi Nakajima-Kimura, and Ms. Ayane Nihashi, for their friendship, help and support at regular intervals.

I am extremely grateful to my previous and current Ph.D. committee members: Dr. Tatsumi Hirata, Dr. Fumi Kubo, Dr. Tsuyoshi Koide, Dr. Akatsuki Kimura, and Dr. Masato Kanemaki for their constant guidance, feedback, and support in my project.

I thank S. Itohara for Rosa26-nls-lacZ (RNZ) mouse (RIKEN BRC:RBRC02657); RIKEN BRC for *Avil*-Cre mouse (RBRC10246); Jackson Laboratories for R26-GCaMP6s mouse (024106).

I am extremely thankful to the Monbukagaku-sho (MEXT) scholarship for supporting me. I am also thankful to the grants that kindly supported this work: JSPS KAKENHI JP20H03346, JP21K18245, JP16H06459 to T.I..

I am immensely grateful to the NIG community, NIG animal facility staff, and specially to Academic Services division of NIG for being exceptionally kind and constantly helping me every step of the way.

I am indebted to my incredible friends, within NIG, outside NIG and those back home in India, without whose constant support, this journey would have been a lot harder.

Last but far from the least, I am eternally grateful to my parents (Mr. Biswajit Banerjee & Mrs. Mala Banerjee), my sister (Ms. Tonima Banerjee), and my extended family, for believing in me and always cheering me on. I could not have done it without them.

Thank you all

Piu Banerjee

FIGURE LEGENDS

Figure 1: Identification of whisker-innervating region in intact TG *ex vivo*

a) Illustration of the mouse whisker-barrel system.

b) Representative image along the dorsal surface of an intact TG from *Avil*-Cre:RNZ mouse at P6. The spatial distribution of peripheral sensory neurons is visualized by X-Gal staining of the whole TG (P6; N= 4 mice). TG outline is shown. M: medial, A: anterior.

c) Schematic for the bacterial artificial chromosome (BAC) construct of Avil-nlsRFP transgenic mouse. The translation initiation site (ATG) of Advillin (Avil) gene on a bacterial artificial chromosome (BAC) clone was replaced with the coding sequence of nuclear localization signal RFP (nlsRFP), and the Amp selection marker was subsequently removed by flp/FRT recombination in bacteria. This BAC construct was microinjected into fertilized eggs to generate Avil-nlsRFP mice.

d) Representative image of an intact TG from *Avil*-nlsRFP mouse at P5. Brightfield (Left), RFP (Middle), Merged (Right) images. (P4–P6; N= 4). e-g) Labeled neuron localization in the P5 TG 5 days after placing DiI crystals around A3 whisker (N= 3) (e), around E3 whisker (N= 3) (f) and lower jaw (N= 3) (g). Brightfield image (Left) and RFP filter image (Right) are shown. Green circles enclose the region of labeled neuron localization.

h) Schematic showing the whisker-row-dependent topography along the dorsal surface of the intact TG.

i) Representative image of the intact TG from the *Avil*-Cre:R26-GCaMP6s mouse at P5. Brightfield image (Left), GCaMP6s image (Middle), Merged image (Right).

j) (Left) Dashed lines indicates where the TG is transected from its peripheral and central connections. (Middle) Schematic of the imaging chamber used for *ex vivo* imaging. An intact TG attached to the cranial base is glued to the base of the chamber. (Right) Schematic of the *ex vivo* imaging setup. The imaging chamber is fixed to the bottom of a 10 cm-diameter petri-dish. The chamber is constantly perfused with buffers and a 20X water immersion lens is used for imaging.

Scale bars: 1 mm

Figure 2: Spontaneous activity in whisker-innervating region of neonatal TG

a) Experimental schematic for performing calcium imaging in a mouse TG *ex vivo.* See Methods for details.

b) A representative raw image frame of *ex vivo* calcium imaging from a total of 600 frames recorded over a period of 10 min (Image 3). The red circles indicate ten exemplary regions of interest (ROIs) of spontaneously firing neurons.

c) Standard deviation image of all 600 frames recorded as indicated in (b). The red circles indicate the same ROIs labelled in (b).

d) Background subtracted ($f-f_o$) images of the red square shown in (b) and (c) at six different timepoints taken at 50 s interval (350^{th} frame to 599^{th} frame).

e) Calcium transients of the ten example ROIs in the 10 min duration. The blue rectangle indicates the range of the timepoints shown in (d) (350^{th} frame to 599^{th} frame).

f) Binary raster plot for the ten example ROIs. Only the calcium transients exceeding the threshold are counted as firing. (Firing threshold: Mean+Std. Dev.).

g) Same image as (b) revealing the ROIs of all the detected spontaneously firing neurons in the 10 min duration. The yellow circles mark individual ROIs. (Total: 73 ROIs).

h) Representative correlation matrix calculated from the fluorescent signals of all the ROI pairs shown in (g) (Firing threshold: Mean+Std Dev). The black squares outline exemplary ROI pairs 23-63 and 49-59, respectively.

i) Fluorescence signals of two example ROI pairs having high correlation (>0.5). The pair shown above (ROIs 23 and 63) are located far (339.3 µm) from each other and the pair shown below (ROIs 49 and 59) are located close (76.4 µm) to each other (see (g)). Correlation matrix of these exemplary ROIs is shown.

j) The plot compares the Pearson's correlation coefficients of all ROI pairs with the distance between them. Each circle represents an individual ROI pair. The dashed vertical line separates the non-correlated ROI pairs (correlation coefficient <= 0.5) from correlated ones. (N= 4 animals).

k) Violin plot showing the distribution of all the correlated and non-correlated ROI pairs based on their inter-ROI distance. The dashed horizontal line represents the median, and the

two dotted lines represent the quartiles. Two-tailed Mann-Whitney test was performed to check for significance (p value<0.0001) (Total non-correlated ROI pairs = 6547, Total correlated ROI pairs = 129, N= 4 animals).

Figure 3: Age-dependent comparison of spontaneous activity in TG

a) Representative images of *Avil*-Cre:R26-GCaMP6s mouse TG across four stages of development (P0–P1, P4–P6, P14–P16, >P60). Top panels show the brightfield images and the bottom panels show the GCaMP6s images. (Scale: 1 mm).

b) Bar graph showing the number of spontaneously firing neurons in a duration of 5 min (Avg. of Images 1, 2, and 3) across the four stages of development. One-way ANOVA with Tukey's multiple comparison test is performed. Each dot represents an individual animal. [P0–P1 (n= 4 animals), P4–P6 (n= 4), P14–P16 (n= 4), >P60 (n= 5)].

c) The first column shows the brightfield image of *Avil*-nlsRFP mouse TG across the four stages of development. The second column shows the RFP^+ area of *Avil*-nlsRFP mouse TGs. The last three columns show regions (L1, L2, L3) of the *Avil*-nlsRFP mouse TG in the *ex vivo* setup. (Scales: 1 mm for first two columns and 100 µm for last three columns).

d) Bar graph representing the number of nuclei (neurons) visible in one locus of *ex vivo* imaging across the four stages of development (Avg. of L1, L2, and L3). One-way ANOVA with Tukey's multiple comparison test is performed. [P0–P1 (n= 4 animals), P4–P6 (n= 6), P14–P16 (n= 6), >P60 (n= 4)].

e) Normalized data of the percentage of neurons firing spontaneously across the four stages of development. In adult stage, <2% neurons fire spontaneously, which is significantly less compared to the remaining three stages. One-way ANOVA with Tukey's multiple comparison test is performed.

f) Raster plots showing spontaneous activity status of 14 randomly selected ROIs in a duration of 5 min at each of the four stages of development. The circle signifies the position of the peak, the line before the circle shows the rise time, and the line following the circle

shows the decay time of individual calcium transients. (Firing Threshold: Mean±Std. Dev.) [P0–P1 (n= 4 animals), P4–P6 (n= 4), P14–P16 (n= 4), >P60 (n= 5)].

g) Comparison of average amplitude of calcium transients across the four stages of development. Kruskal-Wallis test is performed to check for significance. [P0–P1 (n= 870 peaks, 4 animals), P4–P6 (611 peaks, n= 4), P14–P16 (322 peaks, n= 4), >P60 (29 peaks, n= 5)].

h) Comparison of average rise time of calcium transients across the four stages of development. Kruskal-Wallis test is performed to check for significance. [P0–P1 (870 peaks, n= 4 animals), P4–P6 (611 peaks, n= 4), P14–P16 (322 peaks, n= 4), >P60 (29 peaks, n= 5)].

i) Comparison of average decay time of calcium transients across the four stages of development. Kruskal-Wallis test is performed to check for significance. [P0–P1 (702 peaks, n= 4), P4–P6 (501 peaks, n= 4), P14–P16 (258 peaks, n= 4), >P60 (15 peaks, n= 5)].

j) Comparison of average duration of calcium transients across the four stages of development. Kruskal-Wallis test is performed to check for significance. [P0–P1 (702 peaks, n= 4), P4–P6 (501 peaks, n= 4), P14–P16 (258 peaks, n= 4), >P60 (15 peaks, n= 5)].

k) Comparison of average firing events for individual neurons in a duration of 5 min across the four stages of development. One-way ANOVA with Tukey's multiple comparison test is performed. [P0–P1 (n= 359 ROIs, 4 animals), P4–P6 (n= 326 ROIs, 4 animals), P14–P16 (n= 218 ROIs, 4 animals), >P60 (n= 23 ROIs, 4 animals)].

(All error bars: SEM)

Figure 4: Sensory neuron sub-types firing spontaneously in P4–P6 TG

a-b) Representative images showing $CGRP^+$ (a) and $NF\text{-}200^+$ (b) neurons in 20 µm-thick longitudinal sections of mouse TG at P6. Nuclei were stained by DAPI.

c) Distribution of soma-diameter of $CGRP^+$ and $NF\text{-}200^+$ neurons ($CGRP^+$: n= 74 neurons, $NF\text{-}200^+$: n= 75 neurons, 2 animals each). SD, MD, and LD: small, medium, and large-diameter neurons, respectively.

d) Stack images as the sum of all 600 frames recorded over a 10 min duration of *ex vivo* imaging when neurons were subjected to high potassium buffer (Image 4 (I4), L3) for three exemplary ROIs. Diameter of ROIs 1, 2, and 3 is 18.6 µm, 25.5 µm, 18.4 µm, respectively.
e) Scatter plot showing the distribution of neurons activated by high potassium by the diameter of their soma. The lower dashed line represents the boundary of SD and MD neurons (20 µm). The upper dashed line represents the boundary of MD and LD neurons (25 µm). (n= 220 neurons, 2 animals).
f) Stack images as the sum of all 600 frames recorded over a 10 min duration of *ex vivo* imaging when neurons were perfused with EVB (Image 3 (I3), L3) for three exemplary ROIs. Diameters of ROIs 1, 2, and 3 are18.2 µm, 19.0 µm, 26.0 µm, respectively.
g) Scatter plot showing the distribution of spontaneously firing neurons by the diameter of their soma. (n= 76, neurons, 2 animals).
(h) Stacked bar graph comparing the distribution of all neurons and spontaneously firing neurons based on their soma-diameter. The total number of neurons considered is indicated above the bars.
Scale bars: 20 µm

Figure 5: Importance of extracellular calcium in generating spontaneous activity in P4–P6 TG

a) Representative temporal color-coding map showing all spontaneously active neurons in the TG of an *Avil*-Cre:R26-GCaMP6s:*P2RX3*$^{-/-}$ mouse (age: P5) in a duration of 5 min (n= 3).
b) Experimental schematic for testing drugs in *ex vivo* calcium imaging of P4–P6 TG. See the Methods for details. c-f) Temporal color-coding maps showing all spontaneously active neurons in a duration of 5 min (Image 1 (I1)-Left, Image 2 (I2)-Right).
c) Broad purinergic receptor blockers: Suramin (500 µM) + PPADS (100 µM) did not have any obvious effect on spontaneous activity in TG.
d) Broad AMPA/ Kainate/ NMDA receptor blockers: DNQX (100 µM) + D-APV (50 µM) did not have any obvious effect on spontaneous activity in TG.

e) Broad cholinergic/ glycinergic receptor blockers: Atropine (15 µM) + Strychnine (5 µM) did not have any obvious effect on spontaneous activity in TG.
f) Broad GABA-A receptor blocker: Gabazine (100 µM) did not have any obvious effect on spontaneous activity in TG.
g) Representative temporal color-coding map showing the number of spontaneously active neurons in a duration of 5 min before (Image 1) and after (Image 2) perfusion with 0 Ca^{2+} EVB + EGTA (50 mM).
h) Quantitative analysis of the change in the number of spontaneously active neurons following chelation of extracellular calcium (Paired two-tailed t test, p value: 0.0236, N= 3 animals).
Scale bars: 100 µm

Supplementary Figure 1: Labeled neuron localization in P5 TG 5 days after placing DiI crystals around C1 whisker (N= 3) (a), and around C6 whisker (N= 3) (b). Brightfield image (Left) and RFP filter image (Right) are shown. Green circles enclose the region of labeled neuron localization.

Supplementary Figure 2: Binary raster plots showing the reaction of ROIs to high potassium buffer. Only the calcium transients exceeding the threshold are counted as firing events. (Firing threshold: 10*SEM). Fifteen neurons were randomly selected from an animal per age group. [N= 2 animals in each stage].

Supplementary Figure 3: Bar graph representing the size of the RFP+ area in the intact TG of *Avil*-nlsRFP mouse across the four stages of development (Avg. of L1, L2, and L3). Each circle signifies an individual TG. One-way ANOVA with Tukey's multiple comparison test is performed. [P0–P1 (n= 4 animals), P4–P6 (n= 6), P14–P16 (n= 6), >P60 (n= 4)].

Supplementary Figure 4: Expression of *P2RX3* in the developing TG

a) Expression of all the known purinergic receptors in P5 TG and P15 TG analyzed by RNA sequencing. The expression values are given in counts per million (cpm).

b) Expression of *P2RX3* gene in P5 TG, P15 TG, and P5 brain analyzed by qRT-PCR. *GAPDH* is used as a housekeeping gene and *Avil* (Advillin) is used as a sensory neuron-specific gene (n= 2 each) (Error bar: SEM).

Supplementary Figure 5: Generation of *P2RX3* KO mice

a) Schematic describing the construction design for *P2RX3* KO mouse using CRISPR/Cas9. Exon 1 (307 bp) of the *P2RX3* gene is flanked by two designed single guide RNAs (sgRNAs) (64_Forw, 1228_forw) to target that area for deletion. ATG is the translation initiation codon. Location of genotyping primers (OP31/32 and KS253/254) are shown.

b) Representative gel image showing genotyping results for $P2RX3^{+/+}$ (WT), $P2RX3^{-/-}$ (KO), and $P2RX3^{+/-}$ (Het) littermates by PCR with primers (KS253/254).

c) Validation of gene knockout in $P2RX3^{-/-}$ animals by RT-PCR with primers for exons 10-12 (OP19/OP20). TG of P4–P6 $P2RX3^{-/-}$ (KO) and wild-type (WT) littermates were used. *GAPDH* was used as a housekeeping gene.

REFERENCES:

1. Ackman, J. B., T. J. Burbridge and M. C. Crair (2012). "Retinal waves coordinate patterned activity throughout the developing visual system." Nature **490**(7419): 219-225.
2. Aguayo, L. G., B. van Zundert, J. C. Tapia, M. A. Carrasco and F. J. Alvarez (2004). "Changes on the properties of glycine receptors during neuronal development." Brain Research Reviews **47**(1): 33-45.
3. Akhmetshina, D., A. Nasretdinov, A. Zakharov, G. Valeeva and R. Khazipov (2016). "The Nature of the Sensory Input to the Neonatal Rat Barrel Cortex." The Journal of neuroscience : the official journal of the Society for Neuroscience **36**(38): 9922-9932.
4. Ambalavanar, R. and R. Morris (1992). "The distribution of binding by isolectin I-B4 from Griffonia simplicifolia in the trigeminal ganglion and brainstem trigeminal nuclei in the rat." Neuroscience **47**(2): 421-429.
5. Artimovich, E., R. K. Jackson, M. B. C. Kilander, Y.-C. Lin and M. W. Nestor (2017). "PeakCaller: an automated graphical interface for the quantification of intracellular calcium obtained by high-content screening." BMC Neuroscience **18**(1).
6. Babola, T. A., C. J. Kersbergen, H. C. Wang and D. E. Bergles (2020). "Purinergic signaling in cochlear supporting cells reduces hair cell excitability by increasing the extracellular space." eLife **9**.
7. Babola, T. A., S. Li, A. Gribizis, B. J. Lee, J. B. Issa, H. C. Wang, M. C. Crair and D. E. Bergles (2018). "Homeostatic Control of Spontaneous Activity in the Developing Auditory System." Neuron **99**(3): 511-524.e515.
8. Babola, T. A., S. Li, Z. Wang, C. J. Kersbergen, A. B. Elgoyhen, T. M. Coate and D. E. Bergles (2021). "Purinergic Signaling Controls Spontaneous Activity in the Auditory System throughout Early Development." J Neurosci **41**(4): 594-612.
9. Banerjee, P., Kubo, F., Nakaoka, H. et al. Spontaneous activity in whisker-innervating region of neonatal mouse trigeminal ganglion. Sci Rep 12, 16311 (2022).
10. Blankenship, A. G., K. J. Ford, J. Johnson, R. P. Seal, R. H. Edwards, D. R. Copenhagen and M. B. Feller (2009). "Synaptic and extrasynaptic factors governing glutamatergic retinal waves." Neuron **62**(2): 230-241.
11. Bolger, A. M., M. Lohse and B. Usadel (2014). "Trimmomatic: a flexible trimmer for Illumina sequence data." Bioinformatics **30**(15): 2114-2120.
12. Bureau, I., F. von Saint Paul and K. Svoboda (2007). "Correction: Interdigitated Paralemniscal and Lemniscal Pathways in the Mouse Barrel Cortex." PLOS Biology **5**(1): e28.
13. Cabanes, C., M. L. d. Armentia, F. Viana and C. Belmonte (2002). "Postnatal Changes in Membrane Properties of Mice Trigeminal Ganglion Neurons." Journal of Neurophysiology **87**(5): 2398-2407.
14. Cang, J. and D. A. Feldheim (2013). "Developmental mechanisms of topographic map formation and alignment." Annu Rev Neurosci **36**: 51-77.
15. Cantu, D. A., B. Wang, M. W. Gongwer, C. X. He, A. Goel, A. Suresh, N. Kourdougli, E. D. Arroyo, W. Zeiger and C. Portera-Cailliau (2020). "EZcalcium: Open-Source Toolbox for Analysis of Calcium Imaging Data." Frontiers in Neural Circuits **14**.
16. Concordet, J.-P. and M. Haeussler (2018). "CRISPOR: intuitive guide selection for CRISPR/Cas9 genome editing experiments and screens." Nucleic Acids Research **46**(W1): W242-W245.

17. Da Silva, S., H. Hasegawa, A. Scott, X. Zhou, A. K. Wagner, B. X. Han and F. Wang (2011). "Proper formation of whisker barrelettes requires periphery-derived Smad4-dependent TGF- signaling." Proceedings of the National Academy of Sciences **108**(8): 3395-3400.
18. Dooley, J. C., R. M. Glanz, G. Sokoloff and M. S. Blumberg (2020). "Self-generated whisker movements drive state-dependent sensory input to developing barrel cortex." Current Biology **30**(12): 2404-2410. e2404.
19. Erzurumlu, R. S. and S. Jhaveri (1992). "Trigeminal ganglion cell processes are spatially ordered prior to the differentiation of the vibrissa pad." Journal of Neuroscience **12**(10): 3946-3955.
20. Feller, M. B., D. P. Wellis, D. Stellwagen, F. S. Werblin and C. J. Shatz (1996). "Requirement for cholinergic synaptic transmission in the propagation of spontaneous retinal waves." Science **272**(5265): 1182-1187.
21. Ford, K. J., A. L. Félix and M. B. Feller (2012). "Cellular mechanisms underlying spatiotemporal features of cholinergic retinal waves." Journal of Neuroscience **32**(3): 850-863.
22. Galli, L. and L. Maffei (1988). "Spontaneous impulse activity of rat retinal ganglion cells in prenatal life." Science **242**(4875): 90-91.
23. Giovannucci, A., J. Friedrich, P. Gunn, J. Kalfon, B. L. Brown, S. A. Koay, J. Taxidis, F. Najafi, J. L. Gauthier and P. Zhou (2019). "CaImAn an open source tool for scalable calcium imaging data analysis." Elife **8**: e38173.
24. Glowatzki, E. and P. A. Fuchs (2002). "Transmitter release at the hair cell ribbon synapse." Nature neuroscience **5**(2): 147-154.
25. Golshani, P., J. T. Gonçalves, S. Khoshkhoo, R. Mostany, S. Smirnakis and C. Portera-Cailliau (2009). "Internally mediated developmental desynchronization of neocortical network activity." Journal of Neuroscience **29**(35): 10890-10899.
26. Gribizis, A., X. Ge, T. L. Daigle, J. B. Ackman, H. Zeng, D. Lee and M. C. Crair (2019). "Visual Cortex Gains Independence from Peripheral Drive before Eye Opening." Neuron **104**(4): 711-723.e713.
27. Hanganu, I. L., Y. Ben-Ari and R. Khazipov (2006). "Retinal waves trigger spindle bursts in the neonatal rat visual cortex." Journal of Neuroscience **26**(25): 6728-6736.
28. Hashimoto, M. and T. Takemoto (2015). "Electroporation enables the efficient mRNA delivery into the mouse zygotes and facilitates CRISPR/Cas9-based genome editing." Scientific reports **5**(1): 1-8.
29. Hirata, T., T. Kumada, T. Kawasaki, T. Furukawa, A. Aiba, F. Conquet, Y. Saga and A. Fukuda (2012). "Guidepost neurons for the lateral olfactory tract: Expression of metabotropic glutamate receptor 1 and innervation by glutamatergic olfactory bulb axons." Developmental Neurobiology **72**(12): 1559-1576.
30. Iwasato, T. (2020). "In vivo imaging of neural circuit formation in the neonatal mouse barrel cortex." Dev Growth Differ **62**(7-8): 476-486.
31. Iwasato, T., H. Katoh, H. Nishimaru, Y. Ishikawa, H. Inoue, Y. M. Saito, R. Ando, M. Iwama, R. Takahashi, M. Negishi and S. Itohara (2007). "Rac-GAP α-Chimerin Regulates Motor-Circuit Formation as a Key Mediator of EphrinB3/EphA4 Forward Signaling." Cell **130**(4): 742-753.
32. Johnson, S. L., T. Eckrich, S. Kuhn, V. Zampini, C. Franz, K. M. Ranatunga, T. P. Roberts, S. Masetto, M. Knipper and C. J. Kros (2011). "Position-dependent patterning of spontaneous action potentials in immature cochlear inner hair cells." Nature neuroscience **14**(6): 711-717.
33. Jones, T. A., P. A. Leake, R. L. Snyder, O. Stakhovskaya and B. Bonham (2007). "Spontaneous discharge patterns in cochlear spiral ganglion cells before the onset of hearing in cats." Journal of neurophysiology **98**(4): 1898-1908.

34. Kandler, K., A. Clause and J. Noh (2009). "Tonotopic reorganization of developing auditory brainstem circuits." Nat Neurosci **12**(6): 711-717.
35. Katz, L. C. and C. J. Shatz (1996). "Synaptic Activity and the Construction of Cortical Circuits." Science **274**(5290): 1133-1138.
36. Khazipov, R., A. Sirota, X. Leinekugel, G. L. Holmes, Y. Ben-Ari and G. Buzsáki (2004). "Early motor activity drives spindle bursts in the developing somatosensory cortex." Nature **432**(7018): 758-761.
37. Kim, Y. S., M. Anderson, K. Park, Q. Zheng, A. Agarwal, C. Gong, Saijilafu, L. Young, S. He, P. C. Lavinka, F. Zhou, D. Bergles, M. Hanani, Y. Guan, D. C. Spray and X. Dong (2016). "Coupled Activation of Primary Sensory Neurons Contributes to Chronic Pain." Neuron **91**(5): 1085-1096.
38. Kirkby, L. A., G. S. Sack, A. Firl and M. B. Feller (2013). "A role for correlated spontaneous activity in the assembly of neural circuits." Neuron **80**(5): 1129-1144.
39. Kitazawa, T. and F. M. Rijli (2018). "Barrelette map formation in the prenatal mouse brainstem." Curr Opin Neurobiol **53**: 210-219.
40. Kobayashi, Y., Y. Sano, E. Vannoni, H. Goto, T. Ikeda, H. Suzuki, A. Oba, H. Kawasaki, S. Kanba, H.-P. Lipp, N. Murphy, D. Wolfer and S. Itohara (2013). "Genetic dissection of medial habenula–interpeduncular nucleus pathway function in mice." Frontiers in Behavioral Neuroscience **7**.
41. Laumonnerie, C., A. Bechara, N. Vilain, Y. Kurihara, H. Kurihara and F. M. Rijli (2015). "Facial whisker pattern is not sufficient to instruct a whisker-related topographic map in the mouse somatosensory brainstem." Development **142**(21): 3704-3712.
42. Law, C. W., Y. Chen, W. Shi and G. K. Smyth (2014). "voom: Precision weights unlock linear model analysis tools for RNA-seq read counts." Genome Biol **15**(2): R29.
43. Leighton, A. H. and C. Lohmann (2016). "The Wiring of Developing Sensory Circuits-From Patterned Spontaneous Activity to Synaptic Plasticity Mechanisms." Front Neural Circuits **10**: 71.
44. Lennerz, J. K., V. Rühle, E. P. Ceppa, W. L. Neuhuber, N. W. Bunnett, E. F. Grady and K. Messlinger (2008). "Calcitonin receptor-like receptor (CLR), receptor activity-modifying protein 1 (RAMP1), and calcitonin gene-related peptide (CGRP) immunoreactivity in the rat trigeminovascular system: differences between peripheral and central CGRP receptor distribution." J Comp Neurol **507**(3): 1277-1299.
45. Li, H., B. Handsaker, A. Wysoker, T. Fennell, J. Ruan, N. Homer, G. Marth, G. Abecasis and R. Durbin (2009). "The Sequence Alignment/Map format and SAMtools." Bioinformatics **25**(16): 2078-2079.
46. Liao, Y., G. K. Smyth and W. Shi (2014). "featureCounts: an efficient general purpose program for assigning sequence reads to genomic features." Bioinformatics **30**(7): 923-930.
47. Lippe, W. (1994). "Rhythmic spontaneous activity in the developing avian auditory system." Journal of Neuroscience **14**(3): 1486-1495.
48. Maccione, A., M. H. Hennig, M. Gandolfo, O. Muthmann, J. van Coppenhagen, S. J. Eglen, L. Berdondini and E. Sernagor (2014). "Following the ontogeny of retinal waves: pan‐retinal recordings of population dynamics in the neonatal mouse." The Journal of physiology **592**(7): 1545-1563.
49. Madisen, L., A. R. Garner, D. Shimaoka, A. S. Chuong, N. C. Klapoetke, L. Li, A. van der Bourg, Y. Niino, L. Egolf, C. Monetti, H. Gu, M. Mills, A. Cheng, B. Tasic, T. N. Nguyen, S. M. Sunkin, A. Benucci, A. Nagy, A. Miyawaki, F. Helmchen, R. M. Empson, T. Knöpfel, E. S. Boyden, R. C. Reid, M. Carandini and H. Zeng (2015). "Transgenic mice for intersectional

targeting of neural sensors and effectors with high specificity and performance." Neuron **85**(5): 942-958.
50. Marques-Smith, A., D. Lyngholm, A. K. Kaufmann, J. A. Stacey, A. Hoerder-Suabedissen, E. B. Becker, M. C. Wilson, Z. Molnár and S. J. Butt (2016). "A Transient Translaminar GABAergic Interneuron Circuit Connects Thalamocortical Recipient Layers in Neonatal Somatosensory Cortex." Neuron **89**(3): 536-549.
51. Martini, F. J., T. Guillamón-Vivancos, V. Moreno-Juan, M. Valdeolmillos and G. López-Bendito (2021). "Spontaneous activity in developing thalamic and cortical sensory networks." Neuron **109**(16): 2519-2534.
52. Meister, M., R. O. Wong, D. A. Baylor and C. J. Shatz (1991). "Synchronous bursts of action potentials in ganglion cells of the developing mammalian retina." Science **252**(5008): 939-943.
53. Messlinger, K. and A. F. Russo (2019). "Current understanding of trigeminal ganglion structure and function in headache." Cephalalgia : an international journal of headache **39**(13): 1661-1674.
54. Micheva, K. D. and C. Beaulieu (1996). "Quantitative aspects of synaptogenesis in the rat barrel field cortex with special reference to GABA circuitry." J Comp Neurol **373**(3): 340-354.
55. Mizuno, H., K. Ikezoe, S. Nakazawa, T. Sato, K. Kitamura and T. Iwasato (2018). "Patchwork-Type Spontaneous Activity in Neonatal Barrel Cortex Layer 4 Transmitted via Thalamocortical Projections." Cell Reports **22**(1): 123-135.
56. Modol, L., Y. Bollmann, T. Tressard, A. Baude, A. Che, Z. R. S. Duan, R. Babij, N. V. D. M. García and R. Cossart (2020). "Assemblies of perisomatic GABAergic neurons in the developing barrel cortex." Neuron **105**(1): 93-105. e104.
57. Naito, Y., K. Hino, H. Bono and K. Ui-Tei (2014). "CRISPRdirect: software for designing CRISPR/Cas guide RNA with reduced off-target sites." Bioinformatics **31**(7): 1120-1123.
58. Nakazawa, S. and T. Iwasato (2021). "Spatial organization and transitions of spontaneous neuronal activities in the developing sensory cortex." Development, Growth & Differentiation **63**(6): 323-339.
59. Nakazawa, S., H. Mizuno and T. Iwasato (2018). "Differential dynamics of cortical neuron dendritic trees revealed by long-term in vivo imaging in neonates." Nature Communications **9**(1).
60. Nakazawa, S., Y. Yoshimura, M. Takagi, H. Mizuno and T. Iwasato (2020). "Developmental Phase Transitions in Spatial Organization of Spontaneous Activity in Postnatal Barrel Cortex Layer 4." The Journal of Neuroscience **40**(40): 7637-7650.
61. Piñon, M. C., A. Jethwa, E. Jacobs, A. Campagnoni and Z. Molnár (2009). "Dynamic integration of subplate neurons into the cortical barrel field circuitry during postnatal development in the Golli-tau-eGFP (GTE) mouse." The Journal of physiology **587**(Pt 9): 1903-1915.
62. Ran, F., P. D. Hsu, J. Wright, V. Agarwala, D. A. Scott and F. Zhang (2013). "Genome engineering using the CRISPR-Cas9 system." Nature protocols **8**(11): 2281-2308.
63. Scain, A.-L., H. Le Corronc, A.-E. Allain, E. Muller, J.-M. Rigo, P. Meyrand, P. Branchereau and P. Legendre (2010). "Glycine Release from Radial Cells Modulates the Spontaneous Activity and Its Propagation during Early Spinal Cord Development." The Journal of Neuroscience **30**(1): 390-403.
64. Schindelin, J., I. Arganda-Carreras, E. Frise, V. Kaynig, M. Longair, T. Pietzsch, S. Preibisch, C. Rueden, S. Saalfeld, B. Schmid, J.-Y. Tinevez, D. J. White, V. Hartenstein, K. Eliceiri, P. Tomancak and A. Cardona (2012). "Fiji: an open-source platform for biological-image analysis." Nature Methods **9**(7): 676-682.

65. Shen, J. and M. T. Colonnese (2016). "Development of Activity in the Mouse Visual Cortex." J Neurosci **36**(48): 12259-12275.
66. Siegel, F., J. A. Heimel, J. Peters and C. Lohmann (2012). "Peripheral and central inputs shape network dynamics in the developing visual cortex in vivo." Current Biology **22**(3): 253-258.
67. Syed, M. M., S. Lee, J. Zheng and Z. J. Zhou (2004). "Stage‐dependent dynamics and modulation of spontaneous waves in the developing rabbit retina." The Journal of physiology **560**(2): 533-549.
68. Tiriac, A., B. D. Uitermarkt, A. S. Fanning, G. Sokoloff and M. S. Blumberg (2012). "Rapid whisker movements in sleeping newborn rats." Curr Biol **22**(21): 2075-2080.
69. Tomioka, N., N. Osumi, Y. Sato, T. Inoue, S. Nakamura, H. Fujisawa and T. Hirata (2000). "Neocortical Origin and Tangential Migration of Guidepost Neurons in the Lateral Olfactory Tract." The Journal of Neuroscience **20**(15): 5802-5812.
70. Tritsch, N. X., A. Rodríguez-Contreras, T. T. Crins, H. C. Wang, J. G. Borst and D. E. Bergles (2010). "Calcium action potentials in hair cells pattern auditory neuron activity before hearing onset." Nat Neurosci **13**(9): 1050-1052.
71. Tritsch, N. X., E. Yi, J. E. Gale, E. Glowatzki and D. E. Bergles (2007). "The origin of spontaneous activity in the developing auditory system." Nature **450**(7166): 50-55.
72. Valiullina, F., D. Akhmetshina, A. Nasretdinov, M. Mukhtarov, G. Valeeva, R. Khazipov and A. Rozov (2016). "Developmental Changes in Electrophysiological Properties and a Transition from Electrical to Chemical Coupling between Excitatory Layer 4 Neurons in the Rat Barrel Cortex." Front Neural Circuits **10**: 1.
73. Walsh, E. J. and J. McGee (1987). "Postnatal development of auditory nerve and cochlear nucleus neuronal responses in kittens." Hearing research **28**(1): 97-116.
74. Wong, R. O. (1999). "Retinal waves and visual system development." Annual review of neuroscience **22**(1): 29-47.
75. Wong, R. O., A. Chernjavsky, S. J. Smith and C. J. Shatz (1995). "Early functional neural networks in the developing retina." Nature **374**(6524): 716-718.
76. Wong, R. O., M. Meister and C. J. Shatz (1993). "Transient period of correlated bursting activity during development of the mammalian retina." Neuron **11**(5): 923-938.
77. Wu, T. D. and S. Nacu (2010). "Fast and SNP-tolerant detection of complex variants and splicing in short reads." Bioinformatics **26**(7): 873-881.
78. Yamamoto, N. and G. López-Bendito (2012). "Shaping brain connections through spontaneous neural activity." European Journal of Neuroscience **35**(10): 1595-1604.
79. Yang, J.-W., S. An, J.-J. Sun, V. Reyes-Puerta, J. Kindler, T. Berger, W. Kilb and H. J. Luhmann (2013). "Thalamic network oscillations synchronize ontogenetic columns in the newborn rat barrel cortex." Cerebral Cortex **23**(6): 1299-1316.
80. Yang, J.-W., I. L. Hanganu-Opatz, J.-J. Sun and H. J. Luhmann (2009). "Three patterns of oscillatory activity differentially synchronize developing neocortical networks in vivo." Journal of Neuroscience **29**(28): 9011-9025.
81. Zheng, J.-j., S. Lee and Z. J. Zhou (2004). "A developmental switch in the excitability and function of the starburst network in the mammalian retina." Neuron **44**(5): 851-864.
82. Zhou, X., L. Wang, H. Hasegawa, P. Amin, B. X. Han, S. Kaneko, Y. He and F. Wang (2010). "Deletion of PIK3C3/Vps34 in sensory neurons causes rapid neurodegeneration by disrupting the endosomal but not the autophagic pathway." Proc Natl Acad Sci U S A **107**(20): 9424-9429.

FIGURE 1

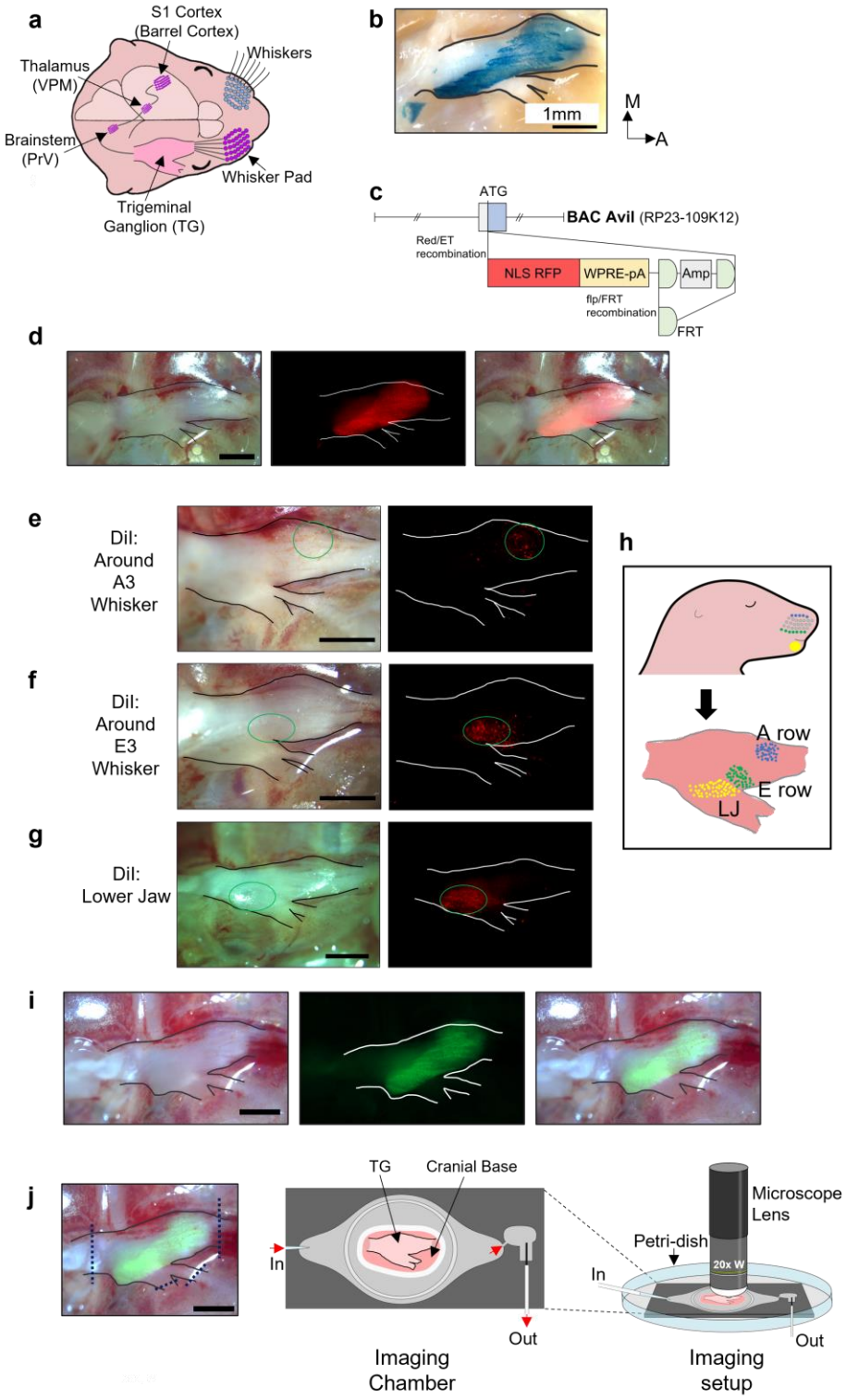
a
S1 Cortex
(Barrel Cortex)
Whiskers
Thalamus
(VPM)
Brainstem
(PrV)
Whisker Pad
Trigeminal
Ganglion (TG)
b
1mm
M
A
c
ATG
BAC Avil (RP23-109K12)
Red/ET
recombination
NLS RFP
WPRE-pA
Amp
flp/FRT
recombination
FRT
d
e
DiI:
Around
A3
Whisker
f
DiI:
Around
E3
Whisker
g
DiI:
Lower Jaw
h
A row
E row
LJ
i
j
TG
Cranial Base
In
Out
Imaging
Chamber
Microscope
Lens
Petri-dish
20x W
In
Out
Imaging
setup

FIGURE 2

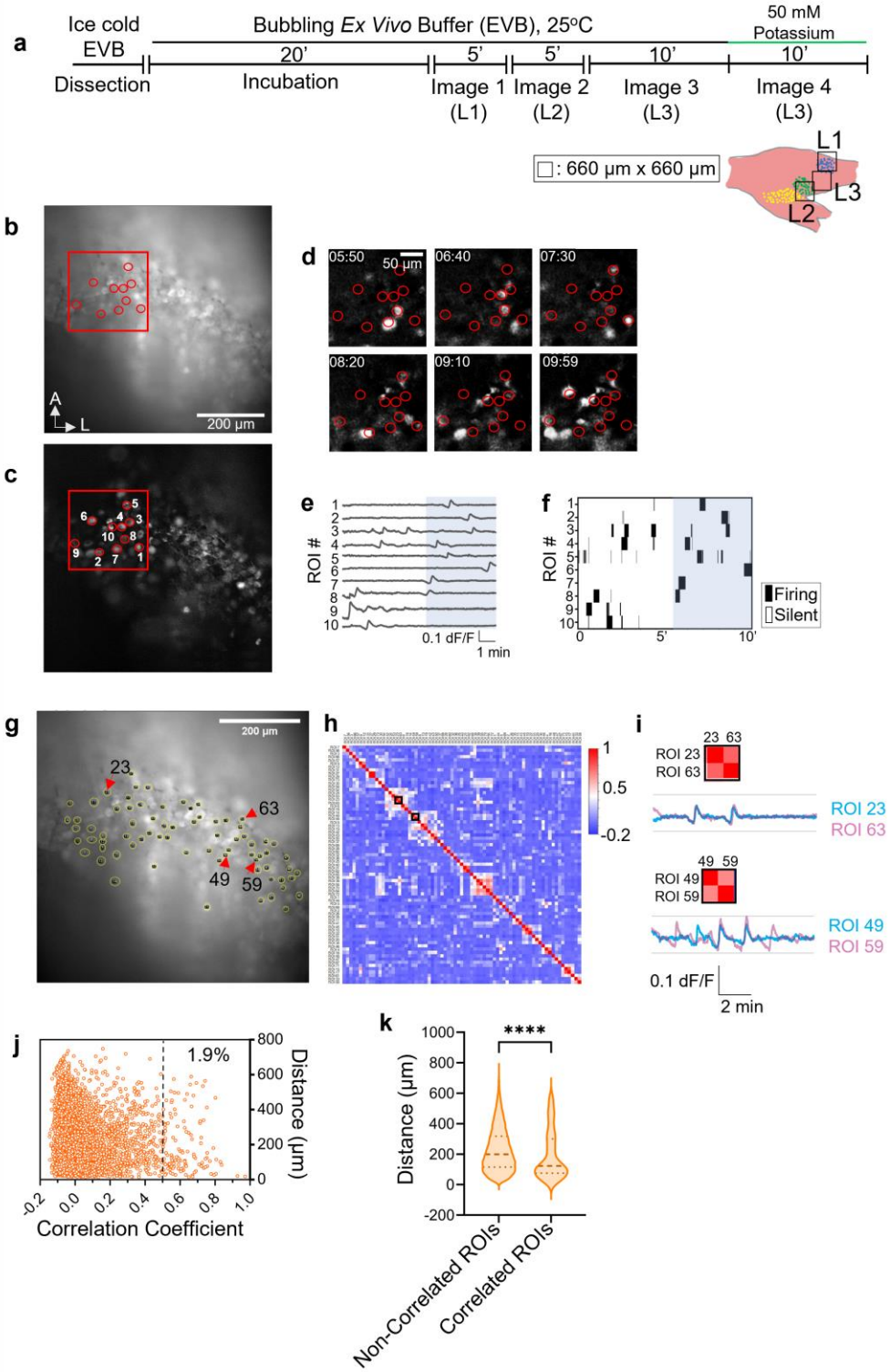
a
Ice cold EVB
Dissection
Bubbling Ex Vivo Buffer (EVB), 25°C
20' Incubation
5' Image 1 (L1)
5' Image 2 (L2)
10' Image 3 (L3)
50 mM Potassium
10' Image 4 (L3)
□: 660 µm x 660 µm
L1
L2
L3
b
200 µm
A
L
c
d
05:50
50 µm
06:40
07:30
08:20
09:10
09:59
e
ROI #
0.1 dF/F
1 min
f
ROI #
Firing
Silent
0
5'
10'
g
200 µm
23
63
49
59
h
1
0.5
-0.2
i
23 63
ROI 23
ROI 63
ROI 23
ROI 63
49 59
ROI 49
ROI 59
ROI 49
ROI 59
0.1 dF/F
2 min
j
1.9%
Distance (µm)
Correlation Coefficient
k
****
Distance (µm)
Non-Correlated ROIs
Correlated ROIs

FIGURE 3

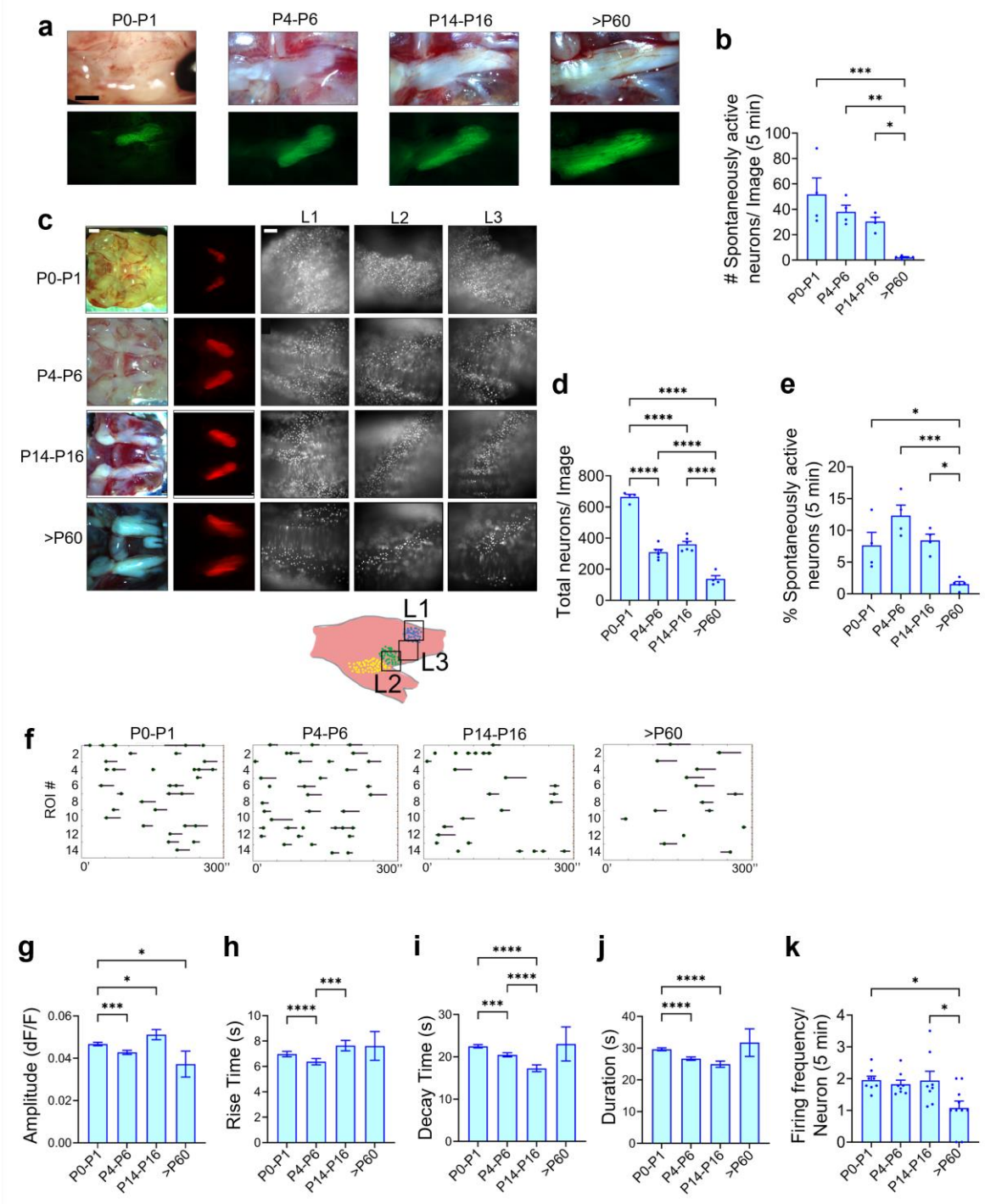
a
P0-P1
P4-P6
P14-P16
>P60
b
Spontaneously active neurons/ Image (5 min)
c
L1
L2
L3
P0-P1
P4-P6
P14-P16
>P60
d
Total neurons/ Image
e
% Spontaneously active neurons (5 min)
f
ROI #
0'
300''
g
Amplitude (dF/F)
h
Rise Time (s)
i
Decay Time (s)
j
Duration (s)
k
Firing frequency/ Neuron (5 min)

FIGURE 4

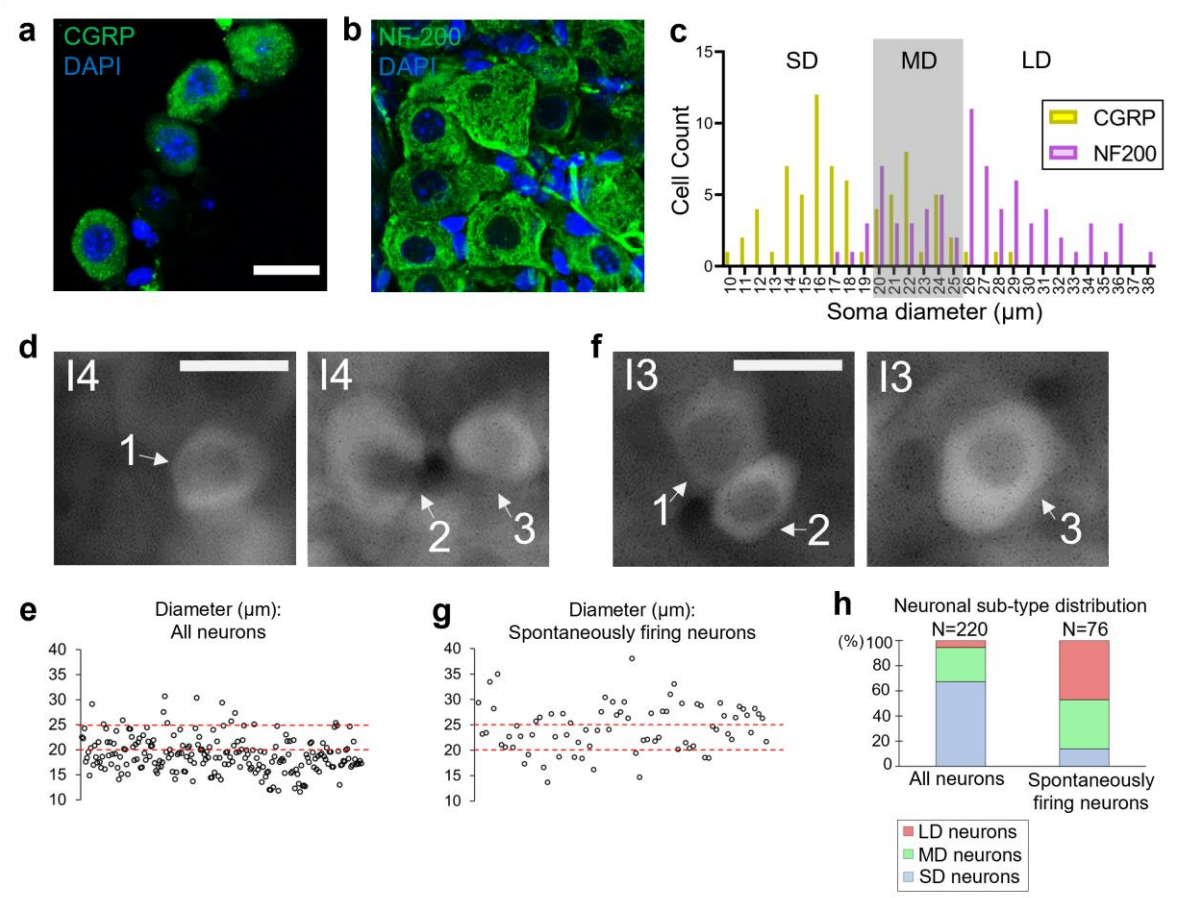
a
CGRP
DAPI
b
NF-200
DAPI
c
SD
MD
LD
CGRP
NF200
Cell Count
Soma diameter (μm)
d
I4
1
I4
2
3
f
I3
1
2
I3
3
e
Diameter (μm):
All neurons
g
Diameter (μm):
Spontaneously firing neurons
h
Neuronal sub-type distribution
N=220
N=76
(%)
All neurons
Spontaneously firing neurons
LD neurons
MD neurons
SD neurons

FIGURE 5

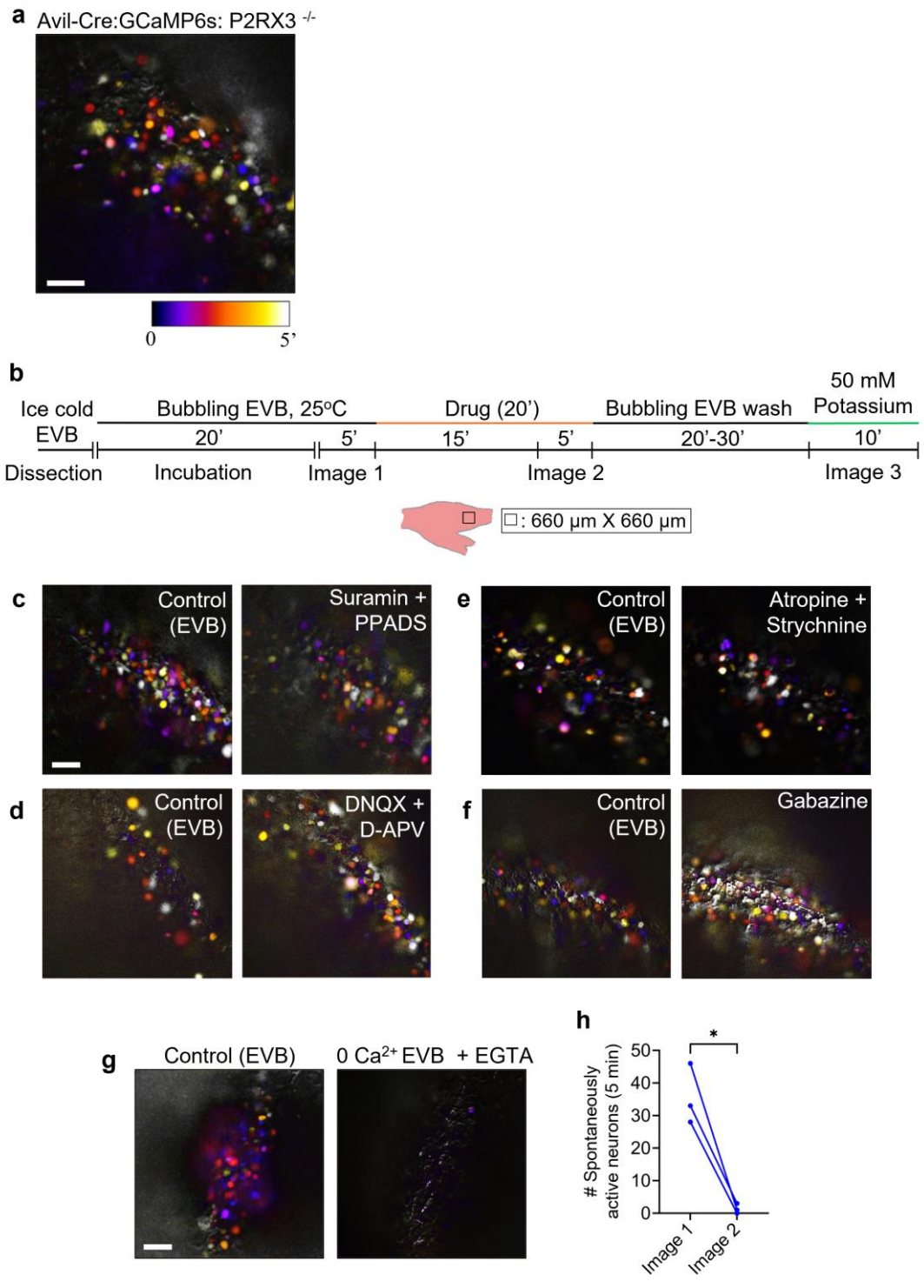
a
Avil-Cre:GCaMP6s: P2RX3 -/-
0
5'
b
Ice cold EVB
Bubbling EVB, 25°C
Drug (20')
Bubbling EVB wash
50 mM Potassium
20'
5'
15'
5'
20'-30'
10'
Dissection
Incubation
Image 1
Image 2
Image 3
□: 660 µm X 660 µm
c
Control (EVB)
Suramin + PPADS
d
Control (EVB)
DNQX + D-APV
e
Control (EVB)
Atropine + Strychnine
f
Control (EVB)
Gabazine
g
Control (EVB)
0 Ca2+ EVB + EGTA
h
Spontaneously active neurons (5 min)
50
40
30
20
10
0
*
Image 1
Image 2

SUPPLEMENTARY FIGURE 1

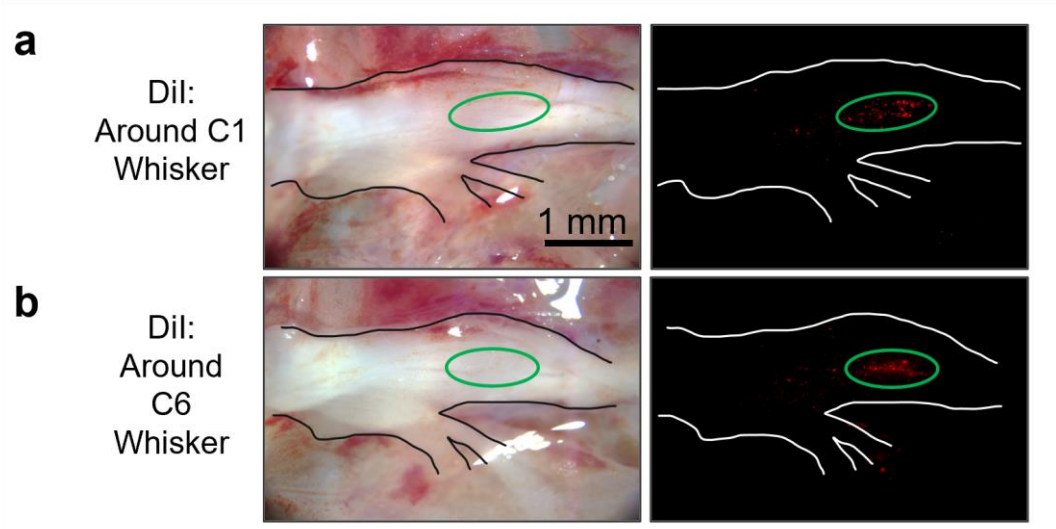

SUPPLEMENTARY FIGURE 2

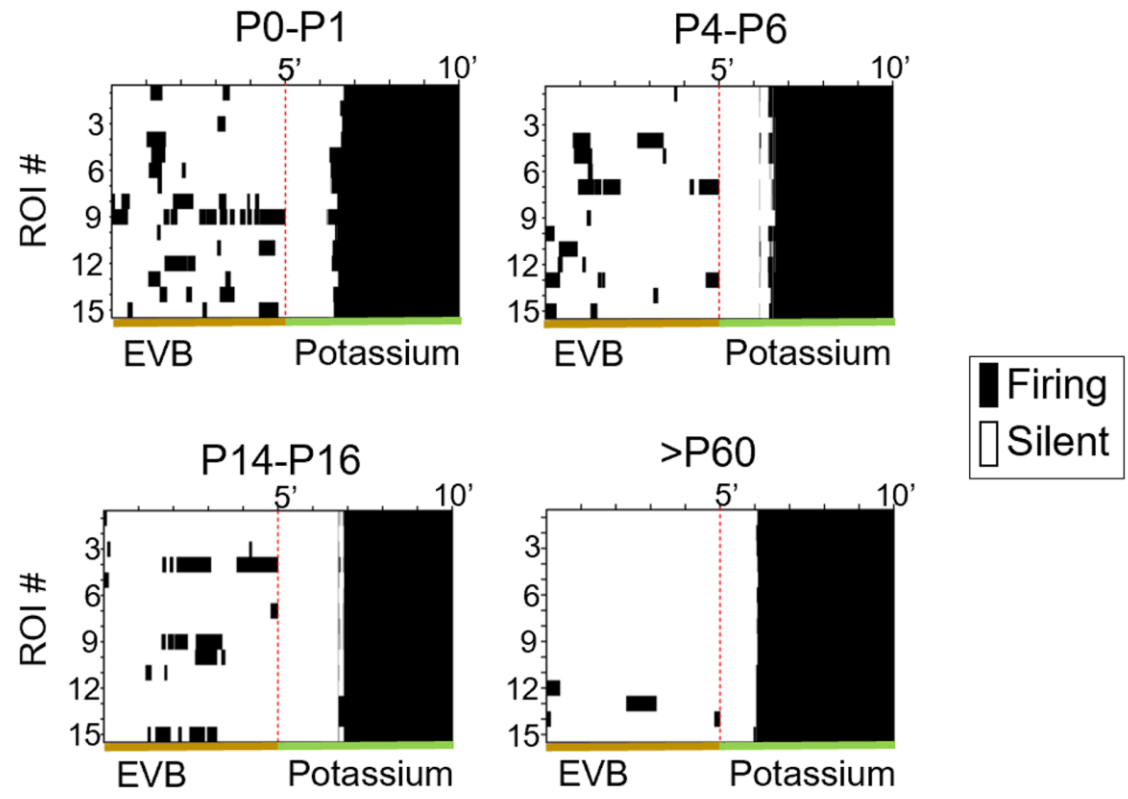

SUPPLEMENTARY FIGURE 3

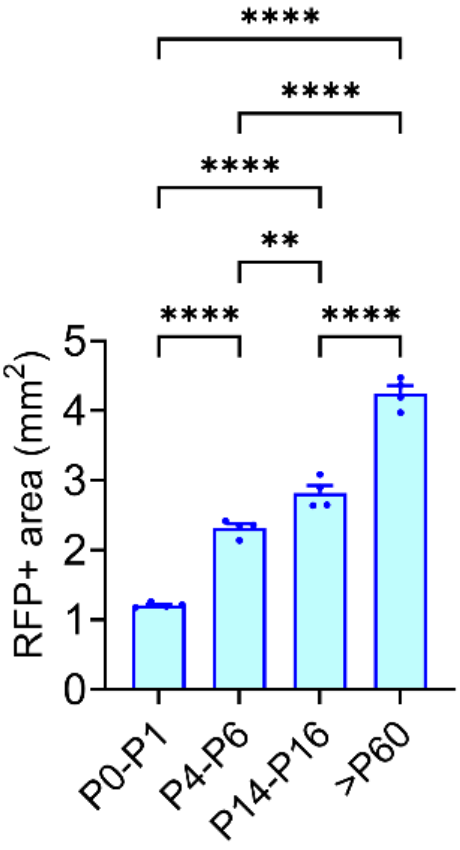

SUPPLEMENTARY FIGURE 4

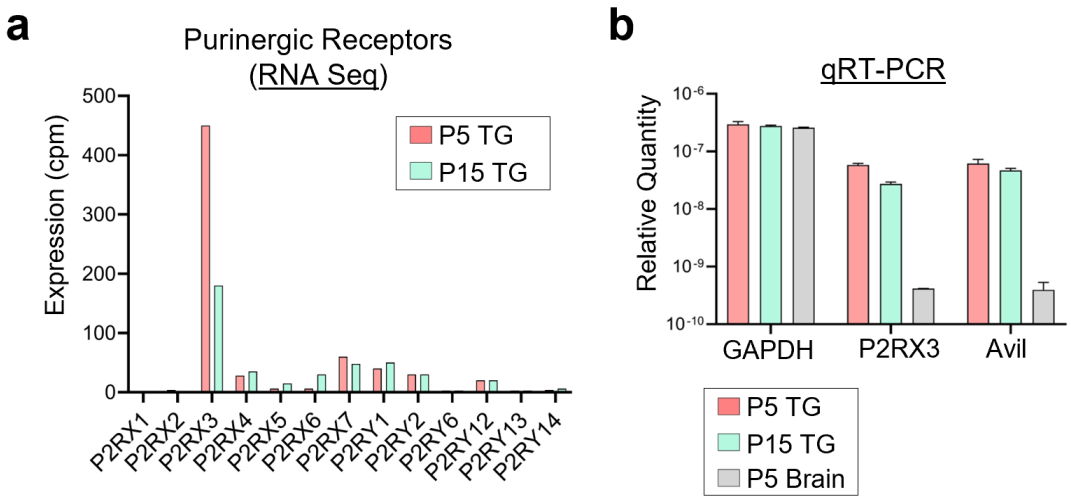

SUPPLEMENTARY FIGURE 5

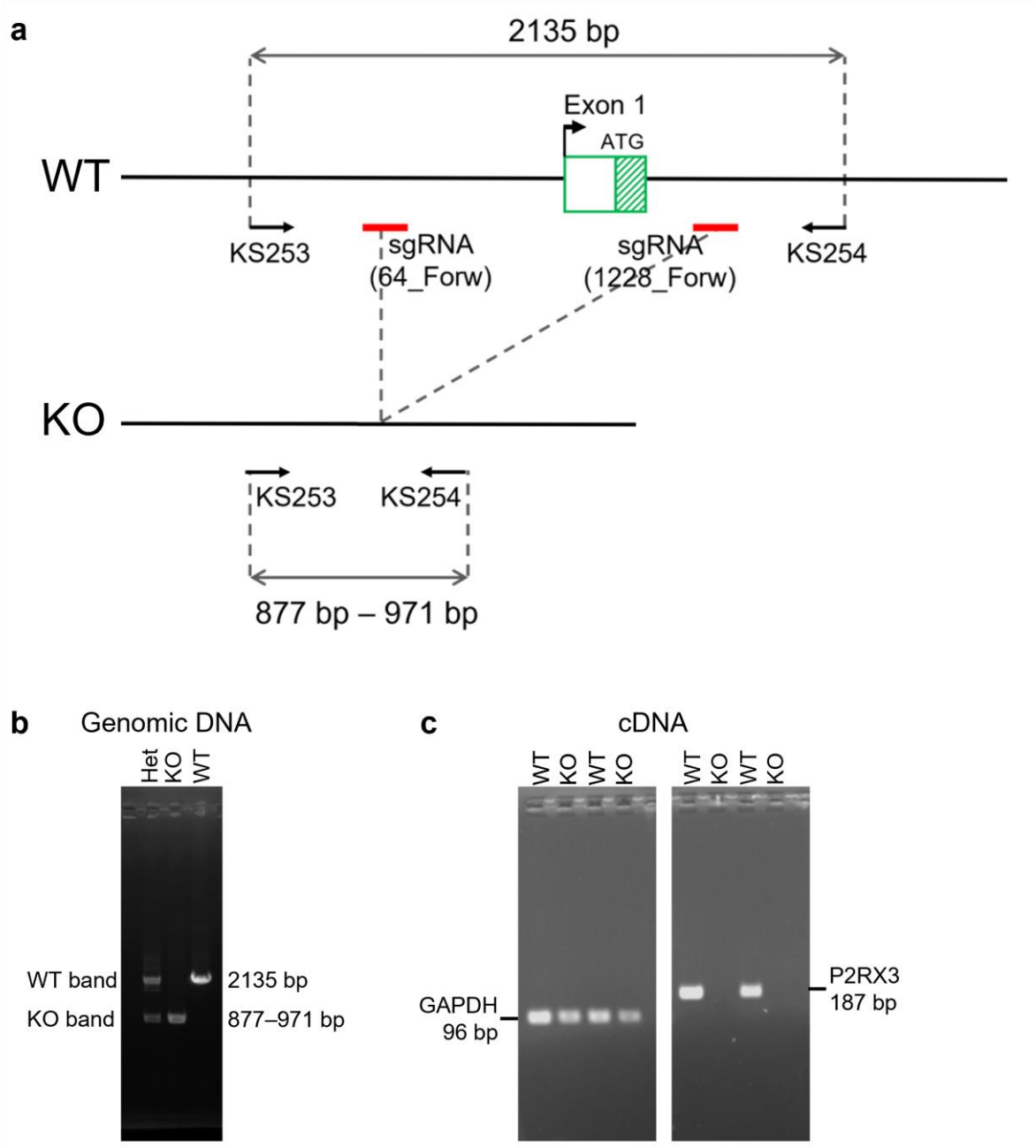

Table 1: Candidate genes expression in developing TG by RNA Sequencing

Category	Gene	P5 TG	P15 TG	Log-2 Fold Change	adj. P. Value
Purinergic Receptors	*P2RX1*	0.84	0.67	0.24	4.94E-01
	P2RX2	4.07	2.31	0.55	1.59E-04
	P2RX3	486.68	180.45	1.45	4.84E-13
	P2RX4	27.13	33.58	-0.41	5.63E-07
	P2RX5	5.73	15.18	-1.49	2.54E-11
	P2RX6	6.32	31.07	-2.37	4.56E-13
	P2RX7	58.75	47.94	0.18	1.51E-01
	P2RY1	44.52	51.06	-0.29	9.84E-04
	P2RY2	27.57	28.50	-0.17	8.59E-02
	P2RY6	3.65	3.45	-0.13	3.45E-01
	P2RY12	16.70	18.48	-0.25	1.50E-02
	P2RY13	3.01	3.37	-0.32	1.74E-02
	P2RY14	4.34	5.74	-0.54	3.76E-05
Glutamatergic Receptors	*GRIA1*	20.70	19.36	-0.01	8.53E-01
	GRIA2	59.99	40.19	0.49	1.64E-06
	GRIA3	31.88	30.73	-0.05	3.65E-01
	GRIA4	76.48	86.87	-0.25	1.32E-03
	GRID1	20.27	20.49	-0.12	5.95E-02
	GRID2	22.44	10.47	0.95	9.52E-08
	GRID2ip	3.10	3.67	-0.37	1.37E-02
	GRIK1	283.55	162.17	0.78	2.91E-09
	GRIK2	22.42	13.73	0.56	7.33E-06
	GRIK3	47.33	30.92	0.50	6.63E-06
	GRIK4	42.95	40.02	0.01	8.94E-01
	GRIK5	80.33	44.80	0.76	9.58E-10
	GRIN1	168.55	121.70	0.42	5.33E-06
	GRINA	232.79	323.65	-0.50	1.47E-07
	GRIN2A	1.44	0.36	1.14	4.60E-06
	GRIN2B	2.28	0.71	1.03	5.19E-04
	GRIN2C	1.34	1.39	-0.12	3.79E-01
	GRIN2D	7.63	2.56	1.27	1.29E-08
	GRIN3A	33.94	20.81	0.59	4.88E-08
	GRM1	1.27	0.85	0.24	4.70E-01
	GRM2	1.27	1.55	-0.33	5.77E-02
	GRM3	4.57	1.49	1.20	2.39E-08
	GRM4	35.70	46.00	-0.46	1.31E-05
	GRM5	5.64	2.72	0.70	7.09E-03
	GRM7	41.42	30.37	0.34	1.12E-03
	GRM8	16.97	17.80	-0.18	1.71E-02
GABAergic Receptors	*GABRA1*	61.31	166.36	-1.50	3.45E-12
	GABRA2	31.67	47.50	-0.67	2.38E-06
	GABRA3	18.71	13.71	0.31	3.00E-03
	GABRA4	8.60	6.24	0.27	1.93E-02
	GABRA5	33.55	24.82	0.31	2.05E-03
	GABRB1	13.92	9.14	0.46	6.53E-04
	GABRB2	15.58	20.28	-0.48	5.21E-04
	GABRB3	147.94	109.36	0.38	2.92E-06
	GABRD	1.14	2.01	-0.69	3.75E-04

	GABRG1	35.95	57.48	-0.76	5.49E-08
	GABRG2	112.62	121.17	-0.15	2.12E-02
	GABRG3	5.87	1.32	1.69	6.53E-09
	GABBR1	410.52	312.15	0.40	5.42E-07
	GABBR2	305.62	227.72	0.39	3.79E-06
Cholinergic Receptors	*CHRM1*	7.96	2.75	1.23	2.27E-08
	CHRM2	26.44	21.65	0.16	1.39E-01
	CHRM3	5.94	4.32	0.23	4.66E-02
	CHRM4	8.70	4.25	0.79	6.48E-08
	CHRNA3	4.23	5.56	-0.54	8.17E-06
	CHRNA4	10.53	3.18	1.44	3.52E-09
	CHRNA5	1.02	0.51	0.53	2.09E-03
	CHRNA6	6.71	32.02	-2.32	1.56E-12
	CHRNA7	21.14	17.89	0.12	3.05E-01
	CHRNB1	1.23	1.45	-0.25	1.31E-01
	CHRNB2	70.15	85.68	-0.37	5.14E-06
	CHRNB3	6.61	12.52	-1.04	4.29E-08
	CHRNB4	2.49	2.98	-0.46	2.01E-02
Glycinergic Receptors	*GLRA2*	5.10	1.55	1.32	9.65E-08
	GLRB	98.08	198.76	-1.06	1.14E-11

Table 2: Calcium channels expression in developing TG by RNA Sequencing.

Categories	Gene	P5 TG	P15 TG	Log-2 Fold Change	adj. P. Value
Cation-Channel Sperm Associated	*CATSPERD*	0.94	0.94	-0.08	6.16E-01
	CATSPERZ	9.18	8.79	-0.07	4.51E-01
	CATSPER2	2.66	4.08	-0.69	3.38E-06
Two-Pore Segment Channel	*TPCN1*	61.91	67.75	-0.21	4.89E-04
	TPCN2	7.64	4.31	0.59	1.36E-06
Voltage-Gated Calcium Channel	*CACNG2*	10.10	17.97	-0.92	2.21E-09
	CACNG3	8.39	3.07	1.16	3.09E-09
	CACNG4	28.16	20.57	0.33	8.02E-04
	CACNG5	86.25	57.05	0.50	9.26E-07
	CACNG7	12.61	16.29	-0.48	2.29E-05
	CACNA1A	108.25	85.68	0.26	3.64E-03
	CACNA1B	172.76	67.18	1.29	1.83E-10
	CACNA1C	55.09	29.83	0.77	9.94E-08
	CACNA1D	18.42	11.26	0.56	8.74E-06
	CACNA1E	8.81	5.15	0.55	1.35E-04
	CACNA1G	21.68	6.01	1.63	1.30E-05
	CACNA1H	76.81	38.30	0.90	4.94E-09
	CACNA1I	4.70	4.79	-0.21	3.58E-02
	CACNA1S	0.84	1.06	-0.30	4.35E-02
	CACNA2D1	145.50	90.85	0.62	1.33E-06
	CACNA2D2	77.05	32.46	1.14	1.91E-11
	CACNA2D3	55.66	76.95	-0.55	1.29E-06
	CACNB1	68.28	45.41	0.50	5.73E-07
	CACNB2	5.89	7.69	-0.52	1.74E-04
	CACNB3	244.93	240.76	0.00	9.67E-01
	CACNB4	111.57	138.06	-0.36	5.06E-05
Ryanodine Receptors	*RYR1*	2.15	1.16	0.59	4.65E-04
	RYR2	29.48	29.36	-0.12	3.64E-01
	RYR3	11.30	8.73	0.22	5.60E-02
Inositol Triphosphate Receptors	*ITPR1*	18.64	24.89	-0.52	1.21E-07
	ITPR2	13.17	8.68	0.40	2.12E-02
	ITPR3	182.17	145.56	0.25	6.45E-02

Table 3: Primer Sequences

Primer ID	Primer Sequence (5' to 3')
KS157 (*Avil* Cre)	CCCTGTTCACTGTGAGTAGG
KS158 (*Avil* Cre)	AGTATCTGGTAGGTGCTTCCAG
KS159 (*Avil* Cre)	TGTTTCACTATCCAGGTTACGGA
KS109 (GCaMP6s)	GTGGACTCATCACGTCGTAAGTGGAATAAG
KS110 (GCaMP6s)	CCAGGGCACGGACAGCTTGCCGGTGG
KS149 (*Avil*-nlsRFP)	GGCACCCAGACCATGAAGAT
KS150 (*Avil*-nlsRFP)	CCAGTTTGCTAGGGAGGTCG
KS253 (*P2RX*3)	TAGCACCGGAGTGCATCTTG
KS254 (*P2RX*3)	GCAACCCCTAGCATGTGTCT
OP31 (*P2RX*3)	CGATCCATTCCGATCGTCCC
OP32 (*P2RX*3)	GATGAGAGGGCAGCCAAGAG
OP11 (*GAPDH*)	CACAATTTCCATCCCAGACC
OP12 (*GAPDH*)	GTGGGTGCAGCGAACTTTAT
OP19 (*P2RX3*)	CTTCCGTGGGAGTGGGGACTGTT
OP20 (*P2RX3*)	GCCCCCGAGTCTGTGGACTGC
OP29 (*Avil*)	GGTCAGTTCCAGGAAGACAG
OP30 (*Avil*)	CTCGTAGAAGTTGCCGTGAG
sgRNA_62Forw	TATTAATGCAGCACGTTTCT
sgRNA_1228Forw	CTCCCATCTAGACCCGTCTC